Abundances of Neutron-Capture Elements in the Galactic Bulge and Disk from High-Resolution Spectra

Rebecca Forsberg

Lund Observatory
Lund University

Thesis for the degree of Licentiate of Philosophy

2021

2021-LIC19

Thesis for the degree of Licentiate of Philosophy
Supervisor: Nils Ryde
March 2021

Lund Observatory
Box 43
SE-221 00 Lund
Sweden

Summary

In the field of research that is often referred to as Galactic archaeology we use the fact that stars act as timestamps of the Galactic interstellar medium from which they are formed. By considering stars of different ages, or metallicities, we can create a timeline for how the Milky Way galaxy has evolved with time. Stars are one of the main constitutes of galaxies, and are found foremost in the central bulge and disk components (if existing in the galaxy). How these components came to be is still not completely clear, and characterization of stars is a useful tool to put constraints on the Galactic evolution.

In this thesis I characterize stars in the Milky Way bulge and bar, in particular by determining their abundances of the so-called neutron-capture elements. I do this by measuring and analysing their stellar spectra. The sample consists of giant stars, 291 from the disk and 45 from the bulge, all observed with high-resolution spectrographs, to get as good data as possible.

In light of the neutron-capture abundances in the stars, I discuss differences and similarities found in the bulge and disk stellar populations. I also compare these with Galactic chemical evolution models, which allow further constraints to be put on the Milky Way evolution. Furthermore, with this work I show that high-precision abundances can be determined from giant stars, which is key for the development of this field.

Contents

Chapter 1

Introduction

The understanding of how different components of galaxies come to be and how they relate to each other, or in other words, the formation and evolution of galaxies, is one of the main topics of research in the field of astrophysics. The Milky Way, our own galaxy, is currently seen as a barred spiral galaxy consisting of multiple components, or *main stellar populations*, often classified as the halo, the thin and thick disks and the bulge. Due to its proximity to us (we are indeed part of the Milky Way), it is in some sense the easiest galaxy to study; we can obtain high-resolution spectra of various classes and types of stars in the different stellar populations of the Galaxy.

Stars have proven to be key to the field of Galactic exploration, since they carry an imprint of the interstellar medium (ISM) from the time at which they were formed. This in turn means that their elemental composition is a timestamp of the elemental composition of that part of the Galaxy from that time. This makes the stars fossils of the Galaxy as it has evolved - a discovery that has given birth to the relatively young field of Galactic archaeology.

Galactic archaeology works under the assumption that the stellar photosphere remains relatively unchanged during the life of the star (Jofré et al., 2019). Thus, observing the photospheres of stars with spectroscopy and determining their chemical compositions using abundance analysis allows for observations of the evolution of the Galactic ISM as it were. This can be compared with Galactic chemical evolution models to draw conclusions on the characteristics of the processes involved in the evolution of the Galaxy, such as time scales and relative importance of different nucleosynthetic channels.

The star formation rate (SFR) and the mass distribution of the stars formed (the initial mass function, IMF, see e.g. Madau & Dickinson (2014)) are key ingredients for understanding the Galactic formation and evolution. Furthermore, well-developed theories and knowledge of stellar structure and evolution is necessary in order to construct models on how stars evolve (Prialnik, 2000). In particular, theories allow us to model the chemical species that are synthesised in stars and later are scattered into the surrounding ISM. Even from simple modeling of the enrichment of the ISM over time we can conclude that the very first stars should have contained only hydrogen, helium and lithium, synthesised in the Big Bang, while progressively younger stars should show higher abundances of heavy elements.

Thus, the chemical composition of stars provides an avenue for exploring the history of the Milky Way and its components; the bulge and disk are the the most stellar-rich components of the Milky Way and are therefore of great interest in Galactic archaeology.

Below I will first introduce and discuss the different main components of the Milky Way (excluding the halo), since we will focus on comparing the bulge with the disks later. Thereafter I will discuss nucleosynthesis with special emphasis on the elements that the thesis is about, namely the neutron-capture process elements. I end this chapter by discussing the paper appended to the thesis, Forsberg et al. (2019).

1.1 The Milky Way Components

The formation and evolution of galaxies is still not well understood; starting from the classical Hubble fork for describing galaxies and their evolution, with spirals merging to create elliptical galaxies, some astronomers believed that the puzzle was solved. However, the fork is today considered to be an extremely over-simplified picture of galaxy evolution and actually not an evolutionary sequence which governs the formation of different galaxies. Thus, the challenge to understand the formation of galaxies and their components resembles that of the chicken and the egg, which one came first, the bulge or the whole galaxy?

1.1.1 The Bulge

From extragalactic observations of galaxies and their bulges, one usually discusses two kinds of bulge, with different formation scenarios (Kormendy & Kennicutt, 2004), being either

- the *classical* scenario where the bulge forms first by mergers of primordial structures, implying that it should be one of the oldest components of the Galaxy. In this scenario the bulge is typically massive compared to the disk, as well as spheroidal and isotropic. Or, it has been proposed that bulges forms by

- secular internal evolution of the disk by gas and stars transferring to the central part, forming, what Kormendy & Kennicutt (2004) call, a *psuedobulge*. These are flatter than the merger-built bulges and have younger stars due to recent starbursts. Due to vertical instabilities, from the formation of a bar, this bulge becomes puffed up and assumes a so-called "boxy/peanut/X"-shape (Shen & Zheng, 2020).

However, it should be noted that some galaxies have been observed to have both a classical as well as a peanut bulge component, indicating that there is no strict grouping between the two cases (Erwin et al., 2015). Additionally, the presence of an X-shape bulge can also be described to solely be a puffed up bar seen from an edge-on angle (see e.g. Bland-Hawthorn & Gerhard, 2016, and references therein). This kind of X-shape bulge originating form a puffed up bar, is usually the picture we have of the Milky Way bulge, as can be seen in Fig. 1.1.

Figure 1.1: Artist's impression showing how the Milky Way galaxy would appear seen almost edge on. The central bulge shows up as a peanut-shaped glowing ball of stars and the spiral arms and their associated dust clouds form a narrow band (ESO/NASA/JPL-Caltech/M. Kornmesser/R. Hurt).

To arrive at a clear understanding of the Galactic bulge provides quite a challenge due to its large coverage of at least 400 deg^2 of heavily extincted sky. The definition of what belongs to the bulge or not varies a lot. A common definition is to use the Galactic coordinates longitude (l) and latitude (b), $(l, b) \leq (|10°|, |10°|)$ (Barbuy et al., 2018), however distance estimates to stars are still cumbersome, making contamination of foreground field stars a problem when observing the bulge.

Nonetheless, we have come to learn quite a lot about the Galactic bulge through detailed chemodynamical studies; the MW bulge has a rather wide spread in metallicity somewhere between -1.5 < [Fe/H] < +0.5 and it is estimated that the bulk of the bulge stellar population is generally older than 10 Gyr (see e.g. Barbuy et al., 2018, and references therein). Although, some studies, i.e Bensby et al. (2017) found that up to 15 % of stars in the MW bulge might be younger than 8 Gyr.

When relating these age-findings to the metallicity distribution functions (MDF) in the bulge, it strongly indicates that the bulge consists of several stellar populations. In general, it seems like the bulk population consists of an older, more metal-poor component that traces a structure more compatible with a spheroid, whilst a more metal-rich component, with younger stars, traces a bar (Zoccali et al., 2008; Babusiaux et al., 2010; Barbuy et al., 2018). To conclude, there are strong indications that both main formation scenarios may have played a role in the formation of the Galactic bulge.

The first attempts to make detailed models of the formation of the Galactic bulge were through chemical evolution models where the fundamental idea was formation on short timescales and a high star formation rate (Matteucci & Brocato, 1990). The high star formation rate has been strongly supported by observations of α-abundances, where the so-called knee in α-abundance over iron-abundance appears to be located at slightly higher metallicities, when compared to the disk. The knee is a result of the onset of iron-production by supernovae type (SNe) Ia, where the metallicity in the bulge has reached higher values before this onset takes place, due to an intrinsic higher star formation rate. Today galaxy formation simulations in a cosmological context are on the verge of producing high-resolution Milky Way analogues, for instance in Agertz et al. (2020) where they combine a hydrodynamic and N-body code to investigate the Milky Ways formation history through its mergers. Thus, models of galactic evolution together with chemodynamical observations have been shown to be a powerful tool for taking further steps in understanding the formation histories of galaxies and our Galaxy.

The Milky Way bulge is still quite a mystery, but there is very strong evidence for the Milky Way to have a typical peanut-shape. Later, this has come to be referred to as the bulge/bar with the bulge having a smooth transition to a bar extended out to a Galactic radius of $R \sim 5$ kpc. The Galactic bulge/bar seem to contain up to ∼30 - 40 % of the Galactic stellar mass (Barbuy et al., 2018), making knowledge about the formation of the bulge/bar a key ingredient in our quest to understand both Galactic and galaxy formation and evolution.

1.1.2 The Disk

The Milky Way disk contains the majority of the stellar mass in the Galaxy (Bland-Hawthorn & Gerhard, 2016), and is, as the name suggest, concentrated at the Galactic mid-plane. It was shown in 1983, by Gilmore & Reid that the local disk need two density profiles to fit the total vertical density distribution of the disk. Following this finding, the two disks have been investigated further and they seem to consist of two distinct stellar populations, distinguished by both chemical abundances, ages and kinematics (see e.g. Bensby et al., 2007, 2014; Adibekyan et al., 2011, 2012). They are often referred to as the thin and the thick disk, originating from the different scale-heights of the disks, where the thin one has a scale height of about 300 pc, whilst the thick disk extends to roughly 1 kpc (Bland-Hawthorn & Gerhard, 2016). The thick disk is also referred to as the high-α disk, the old disk (typically 8 Gyr has been named a separator between the disks) or the kinematically hotter disk; stars belonging to the thick disk have a rotational velocity V which is 40-50 km/s slower than thin disk stars, whilst having higher total velocities $V_{\rm tot} = \sqrt{U^2 + V^2 + W^2}$.

The separation of these two components is however somewhat debated, and there really is no clear cut in either abundances, ages, kinematics nor geometric distribution. Another suggested division of the disk components has been an inner and an outer disk, where it has been shown in Hayden et al. (2015) that the thinner disk indeed stretches further out in the disk than the thick disk (see also the work done in Haywood et al., 2019; Weinberg et al., 2019).

1.2 Nucleosynthesis of elements

One can loosely group the elements of the periodic table according to their astrophysical characteristics, or their production channels, where we have the α-elements, such as oxygen (O), magnesium (Mg) and silicon (Si) (see studies of Reddy et al., 2003, 2006; Adibekyan et al., 2012; Bensby et al., 2014; Jönsson et al., 2017a,b, among others) and the iron-peak elements, such as vanadium (V), chromium (Cr), manganese (Mn), and iron (Fe) (see Battistini & Bensby, 2016; Mikolaitis et al., 2017; Lomaeva et al., 2019, among others). We also have the neutron-capture elements which are the elements heavier than iron. These elements are special in the sense that they are not produced through fusion in stellar processes, since fusion of elements becomes endothermic above iron.

The concept of synthesis of heavier elements through neutron-capture processes was introduced in Burbidge et al. (1957). There are two main physical nuclear reactions involved in the process, namely the capture of neutrons by atomic nuclei and by β-decay. When a neutron is captured by an atomic nuclei, a heavier isotope of that elements is created. This isotope might, or might not, be stable. If it is stable, it can either stay in that state or continue to capture neutrons. Whilst a stable nucleus can go through another neutron capture, an unstable nucleus also has the possibility to undergo a β^-decay, $n \rightarrow p + e^- + \nu$, resulting in an increased proton number and a new, heavier element.

The neutron-capture process is divided into two sub-processes distinguished by the relative time scales of the β-decay and that of the neutron capture, which depends on the neutron flux. These are the so-called slow- and rapid- processes (s- and r-processes), where for the s-process the *beta*-decay time scale is shorter (or *slower*) than the timescale for neutron capture, whilst for the r-process the *rapid* flow of neutrons interacts with the atomic nucleus faster than the time scale of the β-decay. This means that different elements (or rather isotopes) can be reached and produced through the different channels. A descriptive figure and explanation for this is found in Fig. 1.2

So, what sets the conditions for the two processes? The neutron-capture time scale is not constant and depends on a) the local neutron density and b) the neutron absorption cross section of the isotope. The s-process has been shown to require a neutron density of $\leqslant 10^{11}$ cm^{-3} (Busso et al., 1999) and the r-process somewhere between 10^{24} - 10^{28} cm^{-3} (Kratz et al., 2007), allowing constraints to be placed on the environments where these processes can take place.

The neutron densities for the two processes differ by several orders of magnitude and the question of whether there is a third process to fill the intermediate gap has been raised. Indeed, a conceptual intermediate process (i-process) has been proposed, which would have a neutron density around 10^7 - 10^{15} cm^{-3} (Cowan & Rose, 1977; Hampel et al., 2016). This process would possibly give an explanation to the puzzling abundances of carbon-enhanced metal-poor (CEMP) stars in the Galactic halo. These show enrichment in both s- and r-process elements which, due to the various neutron densities, would be produced in different environments. Rapid-accreting white dwarfs (WD) have been the most favoured environment for the i-process to occur (Côté et al., 2018).

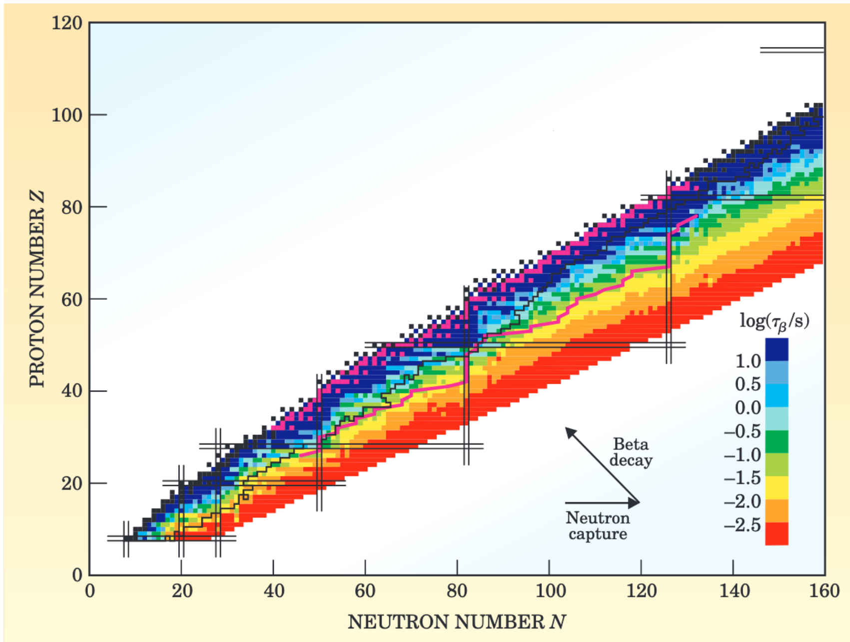

Figure 1.2: This figure shows the map of isotopes. Isotopes stable against β-decay, indicated by the black and magenta boxes, form the valley of stability that runs along the top edge of the band. The different coloured bands indicate decreasing measured or predicted lifetimes with increasing distance from the valley. The jagged black line in the middle is the limit of laboratory information. The magenta line shows a typical path of the r-process, going from a low N,Z to higher N,Z. Such paths tend to turn vertical at the double vertical lines that indicate magic numbers (closed neutron shells in the nuclei). A nucleus on a r-process path eventually β-decays up to the valley of stability to become one of the r-process stable nuclei indicated by the magenta squares. Figure from Cowan & Thielemann (2004), with the courtesy of Peter Möller.

1.2.1 The s-process

The s-process can be divided into three different sub-processes, the weak, main, and strong s-process, that differ solely based on the environment where they take place, and from which nuclear reaction the neutrons originate. The main s-process takes place in the interior of asymptotic giant branch (AGB) stars, which evolved low- to intermediate mass stars (0.5-8 $M_\odot$) (Herwig, 2005). The interior structure of these stars is characterized by a carbon (C) and oxygen core, enclosed by a helium (He) and a hydrogen (H) shell. These shells are separated by the helium intershell, enriched in both helium and carbon.

The helium shells in AGB stars experience instabilities, or thermal pulses (TPs). A TP releases energy which drives convectional flows in the whole intershell for a short period of time. During one of these pulses, partial helium burning occurs, producing a large quantity of ^{12}C.

Then, the third dredge-up (TDU), which occurs when the envelope convection zone extends down to the burning shells, takes place in the AGB star. This brings hydrogen down from the surface to the intershell, causing a ^{13}C-pocket to form in between the burning shells through the following reaction,

$$^{12}\mathrm{C}(p,\gamma)\,^{13}\mathrm{N}(\beta,\nu)\,^{13}\mathrm{C}, \tag{1.1}$$

It is in these ^{13}C-pockets that the s-process nucleosynthesis takes place. The ^{13}C interacts with He-nuclei (i.e α-particles) in the intershell, creating ^{16}O whilst releasing neutrons into the pocket,

$$^{13}\mathrm{C}(\alpha,n)\,^{16}\mathrm{O}. \tag{1.2}$$

Another effect of the dredge-ups, besides the mixing of material, is that products from nucleosynthesis (helium, carbon and s-process) can be brought up to the outer layers of the stellar surface and subsequently blown into the ISM by strong stellar winds, common for AGB stars. An initial stellar mass of 1.5 $M_{\odot}$ has been shown to be the lower mass limit for third dredge-up to take place, by models from Lattanzio (1989) (this means that the Sun will most likely not experience these in the future).

The weak s-process is conceptually very similar to that of the main s-process, but instead of ^{13}C it has another primary neutron source. The neutrons originate from this process,

$$^{22}\mathrm{Ne}(\alpha,n)\,^{25}\mathrm{Mg}, \tag{1.3}$$

which requires higher temperatures than the process in eq. (1.2), consequently taking place at the end of the life-cycles of more massive stars, more specifically in the helium core burning phase and partly in the subsequent convective carbon burning shell phase (Couch et al., 1974). However, it should be noted that this reaction can take place in the most massive AGB stars as well, as discussed in more detail below.

The elements produced by the s-process can further be divided into three different groups: the first, second and third peak s-process elements, defined from the stable nuclei at N = 50 (Sr, Y, Zr), 82 (Ba, La, Ce) and 126 (Hs, Tl, Pb), which results in a build up, or peaks of stable isotopes. The elements found at these peaks have isotopes with low neutron absorption cross sections, which creates bottlenecks in the production of heavier elements, producing an overabundance of stable isotopes. These peaks can be seen in abundance plots against mass number A, such as that in Fig. 1.3.

From findings by Bisterzo et al. (2017), the importance of the size of the ^{13}C-pocket to the s-process production is shown. In the third dredge-up, first-peak s-process elements are created first and, as the neutron exposure increases, the second-peak s-process elements are also created. In AGB stars that are more massive than 4 $M_{\odot}$, the second reaction, eq. (1.3), takes place because of higher temperatures and higher amounts of primary ^{22}Ne (Karakas & Lattanzio, 2014). This increases the neutron density, in addition to shrinking the ^{13}C-pocket. Moreover, the neutron exposure of the reaction ^{22}Ne is lower than that of ^{13}C, resulting in a smaller quantity of s-process elements to be expected, especially the heavier ones. Conclusively, heavier AGB stars produce relatively fewer second peak

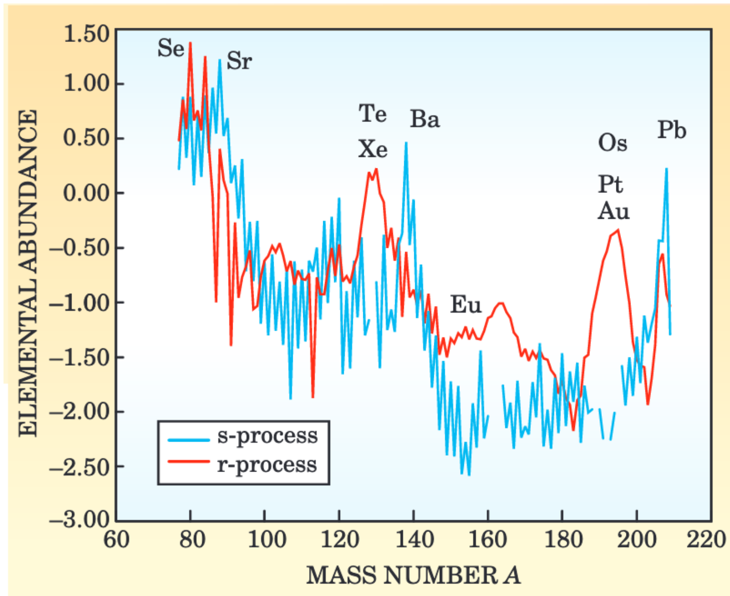

Figure 1.3: This figure shows the abundances of elements produced by s- and r-processes. Abundance peaks are caused by the low neutron-capture rates at magic numbers. Due to the fact that the r-process carries nuclei farther from the valley of stability compared to the s-process, it will encounter the magic numbered shells at lower mass number, causing the general offset between the s- (blue) and r-process (red) peaks. Figure from Cowan & Thielemann (2004).

elements than low-mass AGB stars. Furthermore, at lower metallicities there are fewer Fe seeds available per neutron, meaning that second- (and third-) peak elements are more likely to be produced, compared to first peak elements (Busso et al., 1999).

Due to the intrinsic longer life-times of low to intermediate mass stars compared to more massive stars, there is a time delay for the onset of production of s-process elements, compared to elements synthesised in massive stars. Consequently, any observed s-process-dominated observed element before this onset-time must be due to at least one additional production channel. A non-negligible proportion of the s-process-dominated elements is likely to originate from the r-process at early times (see Fig. 1.4). However, previous models can not, to a full extent, explain the abundance trends of these elements at early times, whereas other possibilities of their origin have been proposed (more on this in the following section).

1.2.2 The r-process

Since the r-process requires a high flux of neutrons, the proposed production sites have been various explosive environments, such as core-collapse supernovae (CC SNe) and the mergers of heavy bodies in binaries, such as neutron star mergers (NSM, Rosswog et al., 1999; Sneden et al., 2000; Thielemann et al., 2011). The presence of neutron star mergers was observationally confirmed by Abbott et al. (2017) as observed by the emission of gravitational waves and the electromagnetic counterpart in the kilonova. Observations of this merger concluded that r-process elements indeed are produced in these highly energetic, neutron rich, mergers (Tanvir et al., 2017; Drout et al., 2017). However, from theoretical calculations the quantity of r-process produced elements in the neutron star merger ejecta depends heavily on the adopted equation of state (Rosswog et al., 2013, 2014; Matteucci et al., 2014), which makes stellar yields hard to constrain for Galactic chemical evolution models.

It has been heavily debated since that discovery whether or not neutron star mergers are the only, or even the dominating, source of r-process elements (see e.g. Côté et al., 2017; Siegel et al., 2018; Duggan et al., 2018; Côté et al., 2019, and discussions therein). In Kobayashi et al. (2020) they find that observed abundance-trends of r-process elements can be reproduced to a large extent if they include yields from magneto-rotational supernovae in their models, whereas the contribution from NSM seem fairly low (see their Fig. 32). Nonetheless, the yields from NSM and especially their possible time-delays, are still fairly uncertain, leaving the r-process production site(s) still not fully constrained.

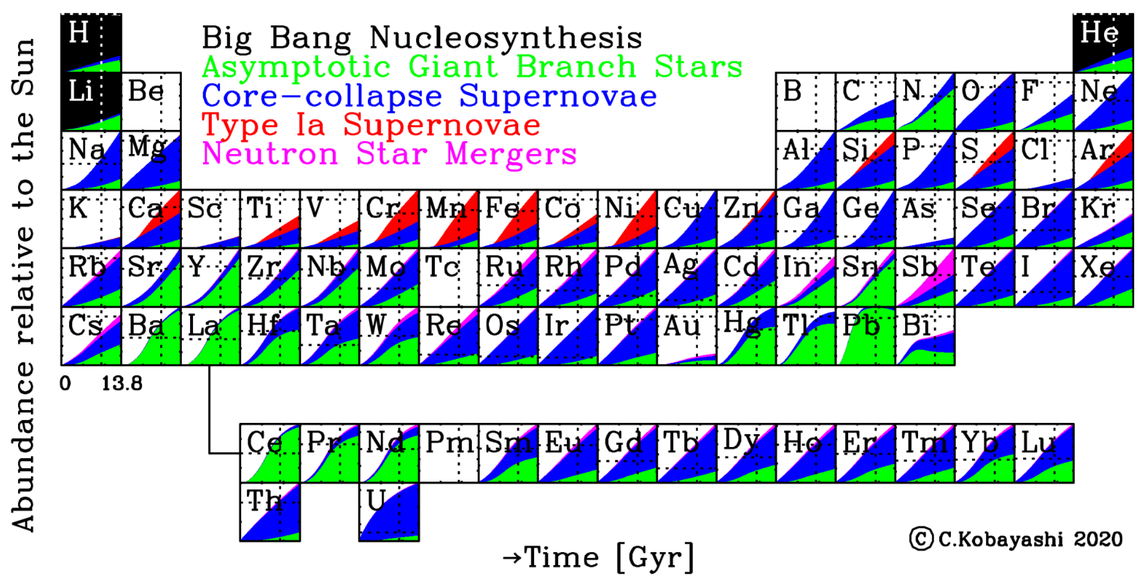

Figure 1.4: Evolution of the elements with time (increasing to the right, in Gyr) in the periodic table. The different colours correspond to formation channels, where Big Bang nucleosynthesis is in black, AGB stars in green, CC SNe (blue, including SNe type II, hypernovae, electron capture SNe, and magneto-rotational SNe), SNe Ia in red, and neutron star mergers in magenta. The dotted vertical and horizontal lines indicate the observed solar values. In this figure one can also see the peaks as portrayed in Fig. 1.3, but here as alternating domination of green and blue, for the s- and r-process respectively. Periodic table from Kobayashi et al. (2020).

The weak r-process

is an additional neutron-capture process introduced as an possible explanation for the large enhancement of the first s-process peak elements Sr, Y and Zr seen in metal-poor stars. Neither yields from the s-process, the r-process or both combined can explain the high abundances, and the weak r-process, or Light Element Primary Process (LEPP) which was introduced by Travaglio et al. (2004).

The site for this proposed process is somewhat debated, but would most likely occur in massive stars, whilst not being directly related to the classical r-process or the weak s-process. However, it should be noted that in Arcones & Montes (2011) they find that SNe with neutron- and proton-rich winds can produce the Sr-Y-Zr peak sufficiently well without the need for a weak r-process. Furthermore, in Trippella et al. (2014) and Cristallo et al. (2015) where they increase the size of the ^{13}C-pocket and include stellar rotation, respectively, they could also produce sufficient Sr-Y-Zr. Similar results, where the contributions from rotating massive stars are included in the s-process, are supported in Prantzos et al. (2018) as well. These results are further strengthened by observations of ultra-faint dwarf galaxies that suggest contribution from rotating massive stars are important for s-process production, especially at low metallicities (Frischknecht et al., 2012, 2016).

However, in Kobayashi et al. (2020) they manage to produce Galactic chemical evolution models that match the observations of the first s-process peak elements without any inclusion from rotating massive stars. Instead they include electron-capture supernovae in addition to AGB stars (which was also successfully considered in Wanajo et al., 2011), although it should be noted that they can not fully reproduce the second s-process peak elements, especially at lower metallicities [Fe/H] < -1 (Fig. 32 in Kobayashi et al.).

1.2.3 Final remarks on neutron-capture nucleosynthesis

There is no clean separation in the periodic table between the s- and r-processes, since both processes can be involved in producing an element, as also seen in the periodic table in Fig. 1.4. However, in general the lighter neutron-capture elements are produced dominantly by the s-process, whilst the contribution from the r-process increases towards higher mass numbers, with some exceptions for very stable elements found at double magic nuclei (N = 50, 82 and 126). Some isotopes are accessible through both s- and r-process paths, whilst some can only be reached through one of the processes. As such, the s-process path goes through more or less all the stable isotopes and ends at ^{209}Bi, due to the low neutron-capture cross section of ^{209}Pb, that decays back to ^{209}Bi, resulting in a blocked loop. To conclude, when one speaks of s- and r-process elements (for instance Ce or Eu, respectively), what really is meant is that those elements have a *dominant* production from either of the processes.

When it comes to the s-process, the main problem to link observations with theoretical models are the yields from various s-process sources. In particular, the ^{13}C-pocket in AGB stars are one of the most significant uncertainties in theoretical modeling, which affects the yield-calculations substantially (Kobayashi et al., 2020). As for the r-process, it is evident both that neutron star mergers exist and produce *some* r-process elements, and that various SNe are important in the production, however the yields for the different sources are yet to be constrained.

1.3 About the Forsberg et al. (2019) paper

Since both s- and r-process elements have different production channels compared to the more studied α- and iron peak elements, these can clearly provide an additional time constraint to the Galactic chemical evolution, especially when disentangling the disks and the bulge. Additionally, the neutron-capture elements comprise more than two thirds of the periodic table of elements, making the study of them crucial in understanding of the full element production throughout the Galaxy and the Universe.

Furthermore, in order to put constraints on the yields from different production channels, it is important to have reliable observational abundances to compare with Galactic chemical evolution models. Previous work on these elements in the disk, for example, Mishenina et al. (2013); Battistini & Bensby (2016); Delgado Mena et al. (2017); Guiglion et al. (2018) used dwarf stars in their studies. Although there are several advantages of working with dwarf stars, they are not as bright as giant stars, limiting the distance at which they can reliably be observed at the same signal-to-noise ratio (S/N), using the same instrumentation.

In Forsberg et al. (2019) we have therefore targeted giant stars and we analyse four neutron-capture elements, namely Zr (first-peak s-process), La, Ce (second-peak s-process) and Eu (r-process), both in the disk and bulge in order to make a differential comparison between the stellar populations of these components. We determined the abundances from high-resolution spectra for a set of 45 bulge stars and 291 disk stars. In Chapter 2 below, I describe details about the observations and stellar sample as well as the method for determining chemical abundances. The results with discussions about the latest work in this field and can be found in Chapter 3

The paper included in this thesis has been published in the scientific journal *Astronomy & Astrophysics* is reproduced with permission from ©ESO. This paper is part of a larger research project that has been ongoing for several years which aims at making differential comparisons of the Milky Way bulge and disk, to help disentangle the formation history of the bulge. As such, this paper the fourth in a series, where stellar parameters, α- and iron-peak-abundances as well as separation between the disk components (thin- and thick) have been determined in the previous ones, see Jönsson et al. (2017a,b); Lomaeva et al. (2019). With this paper, we continue the specialized disk-to-bulge comparison and closed the bulge chapter of that research project.

Lastly, this project is an international collaboration with participation from Francesca Matteucci and her research team from the University of Trieste. Together with them we did a follow up study on the work done here, where Galactic chemical evolution models where adopted to our observational results, see Grisoni et al. (2020). A discussion about this paper is also included in Chapter 3.

Chapter 2

Data and Methodology

2.1 Stellar sample

We are using high-resolution spectra of giant stars to determine abundances of stars found both in the local Galactic disk and in the Galactic bulge. Having high-resolution spectra, using the same atomic lines, same method of analysis as well as the same class of stars in the analysis, allows for a differential comparison of the stellar populations, with minimised systematic uncertainties. In the review paper on the Galactic chemical evolution of the bulge by McWilliam (2016), the necessity of having properly measured abundances for the disk in order to have a reference sample for bulge measurements is stressed. Previous similar work that compares neutron-capture elements in the disk and the bulge compares dwarf and giant stars, respectively (see, for instance Johnson et al., 2012; Van der Swaelmen et al., 2016). An exception is Duong et al. (2019) where they, to as large an extent as possible, use similar stars, atomic data and analysis method as their comparison sample, however the bulge data is indeed analysed separately from the disk data.

One of the main reasons for using giants is due to the fact that they are more luminous than dwarfs, resulting in high-resolution spectroscopic measurements that can not only be obtained at larger distances (such as in the bulge or in the outer disk or halo), but require less observational time at similar distances to that of a given dwarf star. Hence, giant stars can be favorable targets also when working with more "local" Galactic archaeology.

Another reason for having stars of the same type when comparing different stellar populations is the possible elemental depletion found in the photospheres of dwarf stars. Work on atomic diffusion and mixing in stars, see for instance Korn et al. (2007); Lind et al. (2008); Nordlander et al. (2012); Gruyters et al. (2016); Souto et al. (2019); Liu et al. (2019) has shown that evolved stars have systematically higher elemental abundances than dwarf stars, suggesting that abundances measured from dwarf stars are too low. The current favoured explanation is that heavier elements settle into the cores of dwarf stars, depleting the stellar photospheres. These elements are later brought up to the stellar surface due to the increased convective zones in evolved stars.

However, spectroscopic analysis of giant stars is not without its difficulties:

- Giant stars have low effective temperatures ($\sim 3000 - 5000$ K) which enable the formation of molecules in the stellar atmosphere, resulting in spectra with numerous molecular lines. These lines can blend with the atomic lines of interest, which, if not modeled properly, can affect abundance determination. Furthermore, the spectral continuum can be harder to find which can be problematic; abundances are determined by measuring the contrast of the atomic line and continuum opacities. Consequently, a falsely identified continuum will lead to poorly determined abundances, even for high quality data.

- Giant stars typically have low surface gravities, leading to lower electron pressure. As a result, the continuum opacity will be lower, generally increasing the line strength. This increases the risk of saturated lines, which are less sensitive to the abundance and not suitable for abundance determination. However, this effect also strengthens otherwise too weak lines which can not be found in dwarf stars. Some examples are the forbidden [O I] (Jönsson et al., 2017a) and [S I] (Matrozis et al., 2013) lines as well as the HF line (Ryde et al., 2020), which are more favorably measured in giant stars for this reason. For a review of this subject see Chapter 13 in Gray (2005).

Considering these challenges, giant stars require a careful analysis to get proper abundances. Therefore, it is of great importance to find lines that have both good atomic data and are of suitable line strength in the type of star used. The line selection in this project is described in more detail in section 2.2.

2.1.1 Bulge

Our sample of bulge stars consists of 45 giant stars. The spectra of these were obtained with the FLAMES/UVES spectrometer, mounted on the VLT in Chile. Most of the observations took place between May-August in 2003-2004. In Van der Swaelmen et al. (2016) they analysed a total of 56 bulge giants, where 27 of them are re-analyzed in this work. Added to those 27, we have FLAMES/UVES spectra of 18 stars in the Sagittarius Window, observed in August 2011.

In the line-of-sight towards the Galactic bulge the optical extinction of light is quite high due to the large amount of dust, making it quite challenging to observe bulge stars in the optical wavelength region. However, in the bulge sample we have selected stars in fields where the optical extinction is low, whilst still being as close to the centre of the bulge as possible. The bulge fields in this work can be seen in Fig. 2.1.

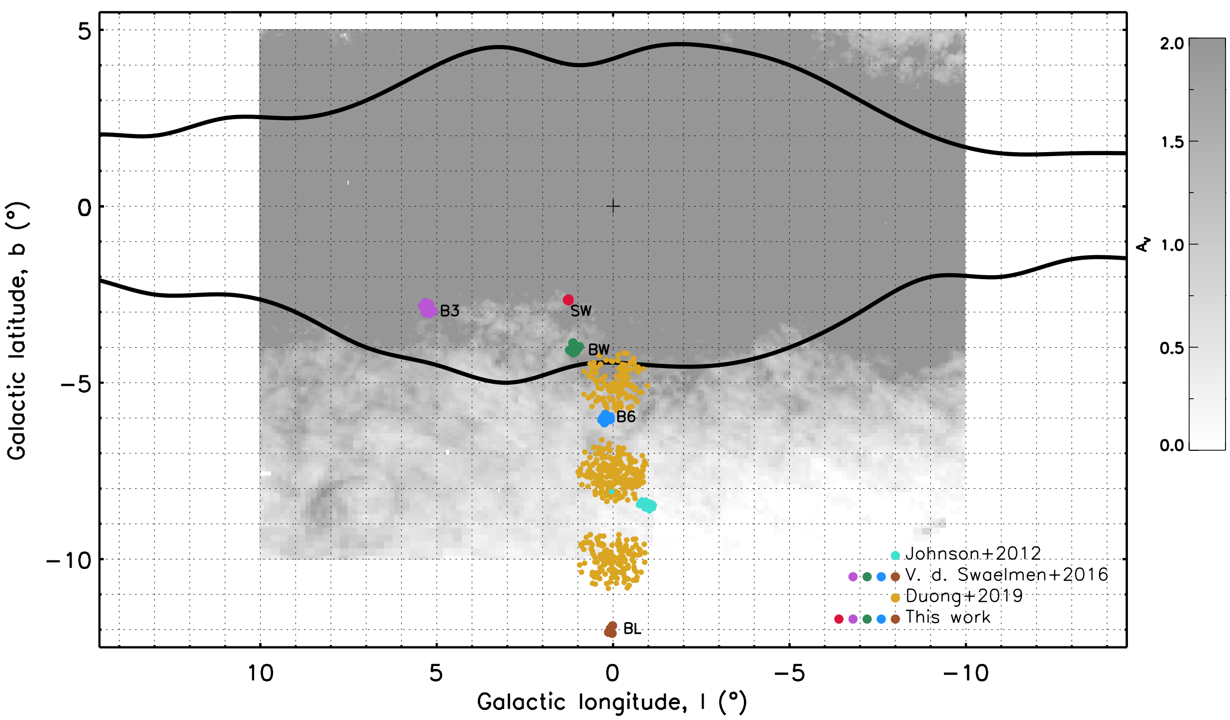

Figure 2.1: Map of the Galactic bulge showing the fields analysed (SW, B3, BW, B6, and BL). Comparison bulge samples from Johnson et al. (2012); Van der Swaelmen et al. (2016) and Duong et al. (2019) can also be seen in the figure. The dust extinction towards the bulge is taken from Gonzalez et al. (2011, 2012) and scaled to the optical extinction (Cardelli et al. 1989). The contours of the Galactic bulge, in black, are from Weiland et al. (1994). Figure reproduced with permission from ©ESO.

2.1.2 Disk

The disk sample consists of 291 giant stars, where a majority of these, 272, have been observed with the FIbre-fed Echelle Spectrograph (FIES Telting et al., 2014) mounted at the Nordic Optical Telescope (NOT), La Palma (see Fig. 2.2). An additional 19 spectra originate from the PolarBase data base (Petit et al., 2014). More details about the observation programmes can be found in Section 2 of the paper.

The bulge and disk spectra are both of high-resolution quality, with resolving powers of R $\sim$ 47 000 and R $\sim$ 67 000, respectively. Even though there is a 20 000 difference in resolution, they both are considered "high", and in the paper we investigated whether or not the higher resolution of the disk spectra made any significant difference to the results, finding this not to be the case.

Due to the wavelength region of FIES extending more widely (4000-7000 Å) than

(a) The outside of the NOT dome at sunset.

(b) The NOT with open dome hatch.

Figure 2.2: Photographs from my first observational visit to the Nordic Optical Telescope (NOT) at Observatorio del Roque de los Muchachos, La Palma, in March 2018.

FLAMES/UVES, we limited the region of interest to 5800-6800 Å in both samples of spectra, to only analyse the same sets of atomic lines in the two stellar samples. This allows us to keep down the systematic uncertainties as much as possible.

2.2 General methodology

The chemical abundances of stars are measured by considering the intensities of the spectral lines of interest for a given chemical species. The abundance relates to the depth and width of the spectral line, and in order to determine the abundance, one needs to know the stellar parameters as well as to properly model the stellar atmosphere were the spectral line formed. In this section I will go through how both parameters and abundances where determined, from the model atmospheres to the selection of spectral lines, estimation of uncertainties, as well as how the separation of the disk stellar populations was done.

We chose to determine both stellar parameters and abundances by synthesizing spectra using the tool Spectroscopy Made Easy (SME, Valenti & Piskunov, 1996; Piskunov & Valenti, 2017). SME allows us to model both blends of lines as well as hyperfine structures, which will be covered more extensively later in this section. To create synthetic spectra, SME requires a set of input parameters, as listed below.

- An observed spectrum.
- A model of the environment where the spectrum is created, i.e the stellar atmosphere. The model describes the temperature and pressure distributions in the star, as a function of (optical) depth. General models of stellar atmospheres are simplified using several assumptions, such as local-thermal equilibrium (LTE) and one

(1) dimension. This both reduces computational time and can decrease the risk for redundant complexity.

- The model atmosphere as generated from the stellar parameters which naturally also are input parameters to SME. The stellar parameters are
  - Effective temperature T_{eff}
  - Surface gravity $log(g)$
  - Metallicity: in this work we have adopted the usual convention of measuring the abundance of an element X in relation to that of the abundance of iron available. Historically, iron has been used since it has a large number of spectral lines at various wavelength regions, and it has come to be one of the better understood elements, from a formation perspective. This makes it a suitable element to compare to. This means that when we refer to the metallicity, it is the stellar iron-to-hydrogen, [Fe/H], that is used. This follows the standard notation of comparing the number density N for a given element (X or Y) of the star to that in the Sun, as

$$[X/Y] = \log_{10}\left(\frac{N_X}{N_Y}\right)_{\text{star}} - \log_{10}\left(\frac{N_X}{N_Y}\right)_{\odot}. \tag{2.1}$$

  - Microturbulence ν_{mic}: this takes into account the small scale, non-thermal motions in the stellar atmospheres. It is introduced in stellar atmosphere modeling and spectral analysis in order to capture non-thermal motions in the stellar atmosphere. These motions are smaller than one mean-free path of the photons and therefore affect the line formation process and the radiative transfer, analogously to thermal motions. In turn, this affects the line strength (see e.g. Gray, 2005). Additionally, there is the macroturbulence ν_{mac} which also is a line broadening mechanism caused by large-scale motions in the atmospheres.

  The stellar parameters were already pre-determined for the stellar sample used in this work by Jönsson et al. (2017a), which the reader is refereed to for a more detailed description. In short, they were determined by using a combination of weak, unblended atomic spectral lines of Fe I, Fe II, Ca I and the wings of three strong Ca I lines which are especially sensitive to the surface gravity.

  Furthermore, SME requires an elemental abundance as an input stellar parameter. In this work this parameter is the only one that is not fixed during the spectral analysis.

- A list of atomic and/or molecular lines. The line list includes data about the transitions, such as the wavelength, ionisation state, lower state excitation energy, oscillator strength and damping parameters. We use the Gaia-ESO line list version 6 (Heiter et al., 2020).

- Lastly, a segment of the spectrum within which a spectral line from the element of interest lies. Usually these segments end up being somewhere between 5-10 Å wide. Within this segment, we mark out the spectral line as well as continuum points in the spectrum, so-called line- and continuum masks. Examples of segments and masks can be seen in both Fig. 2.3 in this Section and in Fig. 2 in Forsberg et al. (2019).

2.2.1 Abundance determination

We chose to determine the abundances of neutron-capture elements, and thus went through all available lines listed in the Arcturus atlas (Hinkle et al., 2000), for each neutron-capture element, within the 5800-6800 Å region.

Finding suitable spectral lines as well as defining the line- and continuum masks is where a majority of the work took place in the making of this paper. I first and foremost followed the recommendations given in the Gaia-ESO line list (Heiter et al., 2020) to select suitable lines, combined with visual inspection of these to select spectral lines that are neither too weak/strong nor too blended with other lines of unknown, or poor, data. I put a lower limit of having at least three (3) continuum masks per segment, with a minimum of one on each side of the spectral line of interest. In order to decrease the workload, this is preliminarily done for all stars simultaneously.

After doing this inspection of all available lines in the observed spectra, we ended up with Zr, La, Ce and Eu as being the elements for which there was atomic data and atomic lines with good enough quality to determine abundances from. Using the given parameters, SME estimates the abundances by using the observed stellar spectra to put constraints on the synthetic spectra. This is done by a weighted χ^2-minimization fit of the spectra (Valenti & Piskunov, 1996).

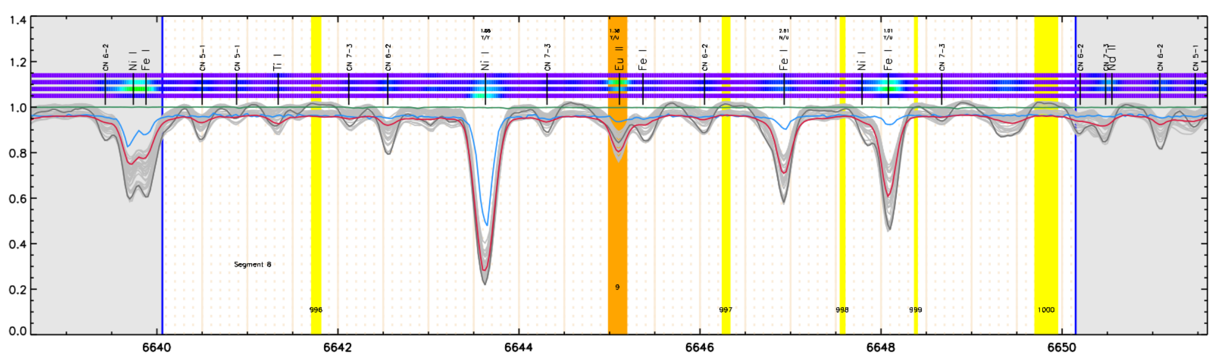

Figure 2.3: Example figure of a spectral line used for abundance determination in this work; the 6645 Å Eu line. The y-axis shows the normalised flux and the x-axis the wavelength. The line of interest is highlighted in orange, whilst continuum is marked with yellow. The vertical blue lines marks the segment. A subset of some roughly normalised disk stellar spectra is plotted in light grey, whilst dark gray and red are the spectra of Rasalas/μLeo and Arcturus/αBoo, respectively. The blue is the Solar spectrum. This figure is reproduced with permission from Forsberg (2019).

Now, both Zr and Eu being odd-Z elements means that they are susceptible to having lines that are split by hyperfine splitting (HFS). These are features that arise due to the odd, and hence, unpaired number of nucleons in the atomic nucleus, causing nucleon-electron spin interactions, which split the atomic energy levels into multiple levels. As a result, what should have been one atomic line in the spectrum due to one transition, is really a multiple line due to multiple transitions. Often these lines are not resolved, but it does nonetheless widen the spectral line.

Another broadening mechanism is that of the isotope shift, which occurs in elements where there is more than one isotope present. Isotopes differ by the number of neutrons in the atomic nucleus, which introduces a shift in both mass and volume of the nucleus, shifting the atomic energy levels as well. The understanding is that an orbital electron will experience a smaller charge per volume/mass from the nucleus, making it less bound. The more massive the atom, the more the isotope shift is dominated by the change of volume rather than the mass. Both Zr, Ce and Eu have more than one isotope available in the stellar atmospheres, which, as well as the hyperfine splitting, has to be properly taken into account in order to get precise abundances.

SME can include hyperfine split lines in the modeling of the synthetic spectra, making it a suitable choice for this work. Unfortunately, the option to include isotope shift of spectral lines is not available in SME, and we instead had to add this manually by scaling the $\log gf$-value of the elements, using the proportion of each isotope in question. The solar isotopic ratios are used for this scaling and the ratios can be found in Table 2 of the paper.

2.2.2 Post-processing and uncertainties

After the synthesized spectra have been produced, they were all manually checked with the observed spectra, in order to make sure that blends as well as spectral wings and depth were modeled properly. Spectra that ended up not being modeled properly, usually due to the low signal-to-noise ratio or strong blending, were not included in the final sample. Finally, the determined abundances were re-normalized to the most up-to-date solar values provided by Grevesse et al. (2015). Additionally, we separated the disk into thin- and thick disk components as well as estimated uncertainties for the abundances, as described below.

Disk separation: As described in 1 Introduction, there is not a clear separation of the disk components and researchers still investigate whether there is in fact a separation or not. Nonetheless, in this work we follow the standard convention of classifying the older, α-rich and kinematically hotter disk as the thick disk, and vice versa. We adopt the separation that was determined in Lomaeva et al. (2019), the third paper of this series. They use a combination of chemistry and kinematics to make the separation, using a clustering method called Gaussian Mixture Model (GMM). The GMM consists of a weighted sum of Gaussian component, which means that the distribution of the combined data are assumed to consist of several Gaussian (sub)distributions. An iterative algorithm calculates the probability that the data points belong to a cluster until the Gaussian parameters converge, where the number of clusters is already known. In Lomaeva et al. (2019) they use abundances of [Ti/Fe] and [Fe/H] from Jönsson et al. (2017a) based on the clear disk separation in titanium. Additionally, they use Gaia DR2 to obtain proper motions (Gaia Collaboration et al., 2018) and distance estimates (McMillan, 2018) that, together with the radial velocities determined in Jönsson et al. (2017a), can be used to calculate the total velocity of the stars. For further details, please refer to Lomaeva et al. (2019).

Uncertainties: Uncertainties can usually be separated into random and systematic ones. Random uncertainties will predominantly arise in our method of determining the stellar parameters, as well as in the placement of the continuum- and line masks. These will depend on the signal-to-noise ratio (S/N) of the spectra. The disk spectra are from bright stellar objects with higher S/N than the bulge spectra, resulting in the uncertainties of the stellar parameters and abundances for the bulge stars strongly dependent upon random uncertainties caused by the lower signal-to-noise.

Systematic uncertainties in the abundances can originate from (incorrect) assumptions about the model atmosphere, uncertainties in the atomic data and also in incorrect stellar parameters. In Jönsson et al. (2017a,b), where our stellar parameters are determined, they investigate how sensitive these are to the S/N as well as compare their determined parameters for some overlapping Gaia Benchmark stars (Jofré et al., 2015). They find that above a S/N > 20 the stellar parameters have high precision, and that the determined parameters shows good agreement with the Benchmark stars. Furthermore, their α-elements in the local disk stars have similar "tightness" (low scatter) in the [α/Fe] over [Fe/H]-plots when compared to previous studies of dwarf stars, pointing at precise stellar parameters.

We have aimed at using the same masks and atomic data for as many of the spectra as possible, this minimises the possibility for systematic uncertainties. Nonetheless, in the Paper we try to estimate the random uncertainties arising from the stellar parameters. We do this by introducing uncertainties in the parameters for Arcturus/α-Boo, a typical giant star in our sample. The uncertainties are generated by Gaussian distributions with a standard deviation of 50 K for the effective temperature, 0.15 dex for $\log(g)$, 0.05 dex for [Fe/H], and 0.1 km/s for the microturbulence, for the disk sample (double for the bulge sample). Then we determined the abundances of the neutron-capture elements of the same Arcturus spectrum, using 500 random combinations of stellar parameters from this recipe. Finally, the abundance uncertainties could be estimated as

$$\sigma A_{\text{parameters}} = \sqrt{|\delta A_{T_{\text{eff}}}|^2 + |\delta A_{\log g}|^2 + |\delta A_{[\text{Fe/H}]}|^2 + |\delta A_{v_{\text{micro}}}|^2}. \quad (2.2)$$

In general, the uncertainties for the disk stars lie around 0.06-0.09 dex, whereas it is, as expected, slightly higher for the bulge stars, around 0.15-0.23 dex. The estimated uncertainties can be seen in Table 3 in Forsberg et al. (2019).

Chapter 3

Results and discussion

After performing the quality selection as described in the last section of the previous chapter, we plot the abundances as [X/Fe] towards [Fe/H] to get the typical evolutionary trend plots, as can be seen in Fig. 3 in Forsberg et al. (2019). This figure shows our overall results, with the disk (thick- and thin) and bulge sample plotted together. It becomes clear from this plot that our disk abundance-trends have a low scatter and that the shape of the s- and r-process elements differs quite a bit. This will be discussed more thoroughly in this chapter.

In the paper we also produced abundance plots using a running mean of the data points. This running mean is accompanied with a running 1σ scatter, which allows us to both assess the general shape of the trends as well as the tightness of these.

In this chapter, I will discuss the [X/Fe]-[Fe/H] plots as well as more comparative plots between the specific abundances, such as the s- and r-process elements La and Eu, respectively, as well as the first- and second s-process peak elements Zr and La+Ce, respectively. This allows for a thorough comparative analysis between the disk and bulge-sample. Lastly, I will tie this work to recent work done in the field and discuss how the Forsberg et al. (2019) paper has contributed to the Galactic archaeology community.

3.1 Comparison with previous work

In Fig. 4 and Fig. 5 of Forsberg et al. (2019) we compare our determined disk abundances with previous work from Battistini & Bensby (2016); Delgado Mena et al. (2017); Mishenina et al. (2013) and Guiglion et al. (2018). In comparison to all of these samples, our estimated uncertainties are smaller, which also can be seen in that we have tighter abundance trends with, in general, less scatter. These literature samples consists of dwarf-stars, since a comparison sample of giant stars with manually determined abundances was (to our knowledge) not available at the time.

In general our observed trends follow similar shapes to the literature comparison samples. We see that the trend for the s-process element Zr is flatter at subsolar metallicities compared to the other two s-process elements La and Ce that have even more of a tilted, banana-like shape. This points at a higher contribution from AGB-stars, which is supported by the models in Kobayashi et al. (2020), see Fig. 1.4 in this thesis. Before the onset of the s-process enrichment by the AGB-star, at around [Fe/H] ~ -0.5 in our results, these elements are created by r-process channels in explosive environments, causing a decrease in [X/Fe] with increasing metallicity. Thus, the r-process element Eu resembles that of an α-element, which is to be expected. See Fig. 8 in Forsberg et al. (2019) where we compare our Eu abundance to the α-element Mg from Jönsson et al. (2017a,b) and find a mostly flat trend for all components.

We note that our [La, Ce, Eu/Fe] in general is supersolar, especially at supersolar metallicities, and are higher than the literature abundances. The reason for this most probably originates from the reported systematic uncertainty of +0.1 dex in the surface gravity from Jönsson et al. (2017a). Indeed, if we consider Fig. 2 in Forsberg et al. (2019), we can see that the lines used to determine the La, Ce and Eu abundances are highly sensitive to the surface gravity. If the surface gravity of a star is determined incorrectly to be too high, this will lead to a synthetic spectral line that is too weak for the "correct" abundance. In order to compensate for this in the spectral analysis to make it match the observed one, SME must increase the abundance, and hence the abundance will incorrectly be determined as too high.

In Fig. 6 in Forsberg et al. (2019) we compare our bulge abundances with previous work from Johnson et al. (2012); Van der Swaelmen et al. (2016) and Duong et al. (2019). A subset consisting of 27 of our bulge spectra has already been analysed in Van der Swaelmen et al. (2016), where in our sample we have added the Sagittarius window (red region in Fig. 2.1) which is closer to the Galactic centre than the previous fields. Furthermore we also determine Zr in this work, which was not done in Van der Swaelmen et al. (2016). In Fig. 6 in the paper we have chosen to compare the running means of the trends rather than the actual data points, due to the higher scatter in the bulge data. This scatter originates from the lower S/N in the spectra, which again is to be expected.

As can be seen in Fig. 6, our bulge trend has a scatter that is comparable to the previous studies, which is reassuring for the quality of the abundances. In general, the shape of the trends is fairly similar to those of the previous studies. We note both that the same possible systematic uncertainties that affect the La, Ce and Eu abundances in the disk, also affect the bulge abundances to be higher than previous studies. Furthermore, we note that our abundances are of high quality with a low scattered trend.

In conclusion, the tightness and general shape-overlap of our abundance trends, points at an efficient determination of giant stellar abundances, both in the Milky Way disk and in the bulge. Since the main purpose of this study is to make a differential analysis between the disk- and bulge stellar populations, any possible systematic uncertainties that generates a systematic offset in our abundances, compared to previous studies, are of less importance.

3.2 Disk and bulge comparison

In Fig. 7 in Forsberg et al. (2019) we compare the (running mean) abundance-trends of the elements with that of the metallicity for the thick-, thin disk and bulge. The overall shape of the trends for the stellar populations are very similar both for the s- and r-process elements (Zr, La, Ce and Eu, respectively). For the s-process elements, [Zr,La,Ce/Fe], the bulge has around ~ 0.1 dex higher abundances, compared with the thick disk, especially at subsolar metallicities. At the same time, the bulge and thick disk trace each other closely in [Eu/Fe]. This suggest that the bulge has a higher fraction of AGB stars than the thick disk, whilst having a similar fraction of massive stars. A difference in IMF could perhaps explain this. Additionally, we observe higher metallicities in the bulge, which could be due to a higher star formation rate, which is suggested in theoretical models (Matteucci et al., 2019). On the other hand, as noted before, the thick disk and bulge trace each-other in [Eu/Fe], which suggests a similar star formation rate between the two populations. Indeed, it is hard to draw any hard conclusions due to the overlapping scatter in the trends.

Comparing two s- and r-process elements (La and Eu in our case) to each other can help disentangle the contribution from the both processes to the formation and evolution of the Galactic components. We have done this in Fig. 9 of Forsberg et al. (2019), which tells us that the r-process dominated the production of the neutron-capture elements at low metallicities, as expected. In general, the [La/Eu] abundances are higher in the bulge compared with the thick disk, once again implying a higher s-process contribution in the bulge, as commented on previously.

In previous papers in this series there are no strong discrepancies in the abundance trends between the (thick) disk and the bulge (Jönsson et al., 2017b; Lomaeva et al., 2019), similar to this paper. A possible shift towards higher metallicities in the bulge for the "α-/SNe type Ia-knee" can not be seen in the α-elements in Jönsson et al. (2017b), nor in our [Eu/Fe], which indeed would strengthen an argument for the bulge having a higher star formation rate compared to the disks.

3.3 Recent work

Since our paper was published, it has principally been used as a comparison sample, both for Galactic chemical evolution models, to the large spectroscopic survey APOGEE and to help put constraints on the cosmic origin to the element fluorine. In this section I will expand on this recent works somewhatt, especially the theoretical paper by Grisoni et al. (2020).

3.3.1 Galactic Chemical Evolution models in Grisoni et al. (2020)

We followed up Forsberg et al. (2019) with a paper in collaboration with Valeria Grisoni, Francesca Matteucci, and their team at the University of Trieste: Grisoni et al. (2020). In this paper we model the evolution of the neutron-capture elements in the Galactic disk and bulge and compare to the observational results.

The Galactic chemical evolution models in Grisoni et al. (2020) build on a few parameters:

- IMF: the initial mass function, governing how many stars of an initial mass that are created. For the bulge one assumes the Sampleter IMF (Salpeter, 1955) that is flatter, or more top-heavy, than the Scalo one (Scalo, 1986) which is assumed in the disk(s). As a result, the bulge will have more massive stars in comparison.
- The star formation rate (SFR).
- Yields for the chemical species:
  - Metallicity: the metallicity comes from core-collapse and type Ia supernovae.
  - s-process: the s-process yields come from stars of masses i.e 1-3 $M_{\odot}$ that end up as low mass AGB-stars and rotation of massive stars as prescribed in Frischknecht et al. (2016).
  - r-process: the yields for the r-process is from a dominant production in NSM, which follows the prescription from Matteucci et al. (2014).

The thin- and thick disks are formed by two in-fall episodes that evolve separately, as introduced in Grisoni et al. (2017). The main difference between the disks, model-wise is that the thick disk has a higher star formation efficiency as well as higher star formation rate. This can be seen in table 1 of Grisoni et al. (2020). The disk model has been tested by Grisoni et al. (2017) and can successfully trace observations of α-elements in both disk components.

The bulge model comes from Matteucci et al. (2019). This model assumes that the bulge has a dominating classical component, whilst acknowledging the presence of a second, younger, more metal-rich component as well.

The results can be seen in their Fig. 1 and Fig. 2 for [Eu/Fe] and [Zr,La,Ce/Fe] against metallicity, respectively. As can be seen in Fig. 1, the model of the bulge traces our bulge abundances well. Although the absolute values of the model abundances are lower than our observed ones in the disk populations, the shapes and separation between the disks seem accurate. Since the thin disk model goes through the solar value at [0,0], the systematic offset between the observed data and model is probably caused by the systematic offset in the observations.

The fact that the bulge is more enhanced in Eu compared to the disk-components in the model, as well as the thick disk to the thin, is a natural result of the higher star formation rate in the bulge and thick disk in the model prescription. In the model, neutron star mergers are set as being the dominant producers of r-process elements (Eu). Today we are not as certain to whether this is true (see e.g. Kobayashi et al., 2020, and references therein) and it becomes apparent to me that we probably need even higher precision abundances in order to put constraints on the models and the r-process production sites.

In Fig. 2 of Grisoni et al. (2020) we see the s-process elements and here the models together with the data are overlapping, but not in such a way that any form of conclusions can be drawn from the results. The models are able to reproduce the banana-like shape in the disks, especially in the thin. The bulge and thick disk have their "onset" of AGB stars at higher [Fe/H] compared to the thin disk, which also makes sense from the modeling point of view, with a more intense star formation rates in these components. However, in the model only yields from low-mass AGB stars are included, which might have a significant effect on the results. As we discuss in Section 5.3 of Forsberg et al. (2019), more massive AGB stars produce more first-peak s-process elements relative to second-peak s-process elements, compared to low-mass AGB stars. Not including the yields from AGB stars more massive than 3 $M_{\odot}$ could be part of the explanation as to why the models do not quite match the observational data.

3.3.2 Origin of fluorine

The cosmic origin of fluorine (F) is still not clear and various sources has been propose as production channels, one of them being AGB stars (Jönsson et al., 2014). With the Ce-abundances in this work we helped to put constraints on the origin of fluorine by comparing Ce, which is produced mainly by AGB stars, with F. We show that the [F/Ce]-[Fe/H] trend is is almost flat in (Ryde et al., 2020), especially at sub-solar metallicities of $-0.6 <$ [Fe/H] < 0.0, although with some scatter. This flat trend points to a similar enrichment time scale and strengthens the argument that AGB stars could be the dominant source of fluorine, at those metallicities.

3.3.3 Comparison sample for APOGEE DR16

In the latest APOGEE DR16 release, (Jönsson et al., 2020) compare their Ce-abundances, determined from infrared spectra on an industrial scale, with our Ce-abundances determined in the disk. We have an overlap of 105 stars with Jönsson et al. (2020) (see their Tab. 12) where these can be seen plotted together in their Fig. 14. Overall, they also find a banana-like shape of the trend, but with a larger scatter than our data.

3.4 Concluding remarks

To conclude this thesis and link back to the introduction, we have in Forsberg et al. (2019) determined abundances for neutron-capture elements in the Galactic bulge and disk, using high-resolution spectra of giant stars. This resulted in high-precision abundances with tight trends in abundance against metallicity plots. The scatter in the bulge trends is higher, due to the lower signal-to-noise in those spectra, which is a natural consequence of the bulge stars being much further away than the local disk stars. Nonetheless, our bulge scatter is comparable, or lower, than previous studies, whereas our disk abundances have lower uncertainties than previous studies. This makes our study one of the more precise ones for comparative analysis of neutron-capture elements in the Milky Way bulge and disk.

In general we find more similarities than discrepancies between our thick disk and bulge, pointing at a similar formation history. This is especially true for the s-process elements, with the exception being that [La/Fe] is 0.1 dex higher in the bulge, which would suggest that the bulge would have a different IMF than the local disk. From the comparison with Galactic chemical evolution models in Grisoni et al. (2020), we find that [Eu/Fe] is enhanced in the bulge compared to the thick disk, however this is still within our reported uncertainties in the observations, so we refrain from making any firm claims. Nonetheless, it is interesting that our observations nicely fits the proposed formation model of the bulge in Grisoni et al. (2020), namely for Eu.

From this work, we can clearly see that the neutron-capture elements are important to arravining at a complete picture of the Galactic chemical evolution. These elements make up a majority of the elements in the periodic table and can tell a story which other elements fail to tell, namely that of AGB-stars, neutron star mergers and to some extent, details of the metal-poor Galaxy with rotating massive stars.

The future

In spite of mudh progress, both observationally and theoretically, it is evident that we still do not have a complete picture of the Milky Way's formation history nor a full understanding of how the different Galactic components came to be. With help from large Galactic spectroscopy surveys, such as GALAH, LAMOST, and APOGEE and upcoming optical WEAVE, 4MOST, and near-IR MOONS, in combination with Gaia, the chemodynamical picture of the Milky Way will, hopefully, become much clearer. The aforementioned large spectroscopic surveys all determine their stellar parameters and chemical abundances using pipelines, resulting in industrially determined abundances. For very large data-sets, the task to determine abundances manually truly is a too time-consuming task, however, it is nonetheless important that these industrial abundances can be compared to high-quality ones determined in a careful way.

To extend the disk-sample presented in this work, I have participated in collecting more spectra of giant stars, giving a sample of more than 500 spectra of local disk stars. Together with Jönsson et al. (in prep) we will present a reference sample of these Giant stars In the Local Disk (or GILD). This sample will have precise stellar parameters (addressing the systematic uncertainties in the surface gravity from Jönsson et al., 2017a) and since we can use the whole wavelength range of FIES, 4100 - 7360 Å, more lines will be available for the abundance determination, compared to what was used in this thesis, increasing the precision of the determined abundances. This additionally allows us to determine abundances for over 25 chemical species, making the GILD sample both a reference sample towards industrial abundances of giant stars as well as a reference of the local Galactic disk.

A natural step for Galactic research to take is to move towards the infrared part of the spectra. Infrared radiation can, to a higher extent, penetrate the dust-covered areas of the Galactic disk and bulge/bar, making it possible to observe otherwise inaccessible (to optical observations) regions of the Galaxy such as the Galactic nucleus. This is key for gaining a better understanding of the various Galactic stellar populations. APOGEE has successfully derived abundances for 26 elements using the H-band, however this field of working with stellar spectra in the infrared is still under development and will be continued, partly with near-infrared spectrograph MOONS on VLT, that will work in a similar wavelength regime as APOGEE. Although this regime will be slightly narrower, and with a 20% lower spectral resolution, it will be more efficient with a larger amount of fibers and from a larger telescope. The challenges they confront of are similar to those that have already been, to a large extent, overcome by the optical community, having knowledge about usable lines for parameter and abundance determination. Our sample of precise data from optical spectra will play, and already have played, a role in evaluating results from the infrared field (Jönsson et al., 2020)

Nonetheless, even though APOGEE has successfully measured Ce, the best analysis options for getting abundances of (known) neutron-capture elements lie in the optical wavelength regime, due to lack of neutron-capture element spectral lines in these instruments' wavelength coverage's. Thus, for the future the best survey is 4MOST for the bulge, however it will not probe very deeply and roughly beyond 3-4 degrees from the plane, thus avoiding the dust obscure Galactic plane. As such, our sample of neutron-capture elements for bulge giants is to this date, and for the near future, one of the most precise samples there is for these elements.

Bibliography

Abbott, B. P., Abbott, R., Abbott, T. D., et al. 2017, Phys. Rev. Lett., 119, 161101

Adibekyan, V. Z., Santos, N. C., Sousa, S. G., & Israelian, G. 2011, A&A, 535, L11

Adibekyan, V. Z., Sousa, S. G., Santos, N. C., et al. 2012, A&A, 545, A32

Agertz, O., Renaud, F., Feltzing, S., et al. 2020, arXiv e-prints, arXiv:2006.06008

Arcones, A. & Montes, F. 2011, ApJ, 731, 5

Babusiaux, C., Gómez, A., Hill, V., et al. 2010, A&A, 519, A77

Barbuy, B., Chiappini, C., & Gerhard, O. 2018, ARA&A, 56, 223

Battistini, C. & Bensby, T. 2016, A&A, 586, A49

Bensby, T., Feltzing, S., Gould, A., et al. 2017, A&A, 605, A89

Bensby, T., Feltzing, S., & Oey, M. S. 2014, A&A, 562, A71

Bensby, T., Zenn, A. R., Oey, M. S., & Feltzing, S. 2007, ApJ, 663, L13

Bisterzo, S., Travaglio, C., Wiescher, M., Käppeler, F., & Gallino, R. 2017, ApJ, 835, 97

Bland-Hawthorn, J. & Gerhard, O. 2016, ARA&A, 54, 529

Burbidge, E. M., Burbidge, G. R., Fowler, W. A., & Hoyle, F. 1957, Reviews of Modern Physics, 29, 547

Busso, M., Gallino, R., & Wasserburg, G. J. 1999, Annual Review of Astronomy and Astrophysics, 37, 239

Côté, B., Belczynski, K., Fryer, C. L., et al. 2017, ApJ, 836, 230

Côté, B., Denissenkov, P., Herwig, F., et al. 2018, ApJ, 854, 105

Côté, B., Eichler, M., Arcones, A., et al. 2019, ApJ, 875, 106

Couch, R. G., Schmiedekamp, A. B., & Arnett, W. D. 1974, ApJ, 190, 95

Cowan, J. J. & Rose, W. K. 1977, ApJ, 212, 149

Cowan, J. J. & Thielemann, F.-K. 2004, Physics Today, 57, 10.47

Cristallo, S., Abia, C., Straniero, O., & Piersanti, L. 2015, ApJ, 801, 53

Delgado Mena, E., Tsantaki, M., Adibekyan, V. Z., et al. 2017, A&A, 606, A94

Drout, M. R., Piro, A. L., Shappee, B. J., et al. 2017, Science, 358, 1570

Duggan, G. E., Kirby, E. N., Andrievsky, S. M., & Korotin, S. A. 2018, ApJ, 869, 50

Duong, L., Asplund, M., Nataf, D. M., Freeman, K. C., & Ness, M. 2019, MNRAS, 486, 5349

Erwin, P., Saglia, R. P., Fabricius, M., et al. 2015, MNRAS, 446, 4039

Forsberg, R. 2019, Detailed chemical abundances of neutron-capture elements - from 523 local giant stars, student Paper

Forsberg, R., Jönsson, H., Ryde, N., & Matteucci, F. 2019, A&A, 631, A113

Frischknecht, U., Hirschi, R., Pignatari, M., et al. 2016, MNRAS, 456, 1803

Frischknecht, U., Hirschi, R., & Thielemann, F. K. 2012, A&A, 538, L2

Gaia Collaboration, Brown, A. G. A., Vallenari, A., et al. 2018, A&A, 616, A1

Gilmore, G. & Reid, N. 1983, MNRAS, 202, 1025

Gray, D. F. 2005, The Observation and Analysis of Stellar Photospheres, 3rd edn., Vol. 3 (Cambridge University Press, The Edingburgh Building, Cambride CB2 8RU, UK: Cambridge University Press), ch. 13, p. 327

Grevesse, N., Scott, P., Asplund, M., & Sauval, A. J. 2015, A&A, 573, A27

Grisoni, V., Cescutti, G., Matteucci, F., et al. 2020, MNRAS, 492, 2828

Grisoni, V., Spitoni, E., Matteucci, F., et al. 2017, MNRAS, 472, 3637

Gruyters, P., Lind, K., Richard, O., et al. 2016, A&A, 589, A61

Guiglion, G., de Laverny, P., Recio-Blanco, A., & Prantzos, N. 2018, A&A, 619, A143

Hampel, M., Stancliffe, R. J., Lugaro, M., & Meyer, B. S. 2016, ApJ, 831, 171

Hayden, M. R., Bovy, J., Holtzman, J. A., et al. 2015, ApJ, 808, 132

Haywood, M., Snaith, O., Lehnert, M. D., Di Matteo, P., & Khoperskov, S. 2019, A&A, 625, A105

Heiter, U., Lind, K., Bergemann, M., et al. 2020, arXiv e-prints, arXiv:2011.02049

Herwig, F. 2005, ARA&A, 43, 435

Hinkle, K., Wallace, L., Valenti, J., & Harmer, D. 2000, Visible and Near Infrared Atlas of the Arcturus Spectrum 3727-9300 A

Jofré, P., Heiter, U., & Soubiran, C. 2019, ARA&A, 57, 571

Jofré, P., Heiter, U., Soubiran, C., et al. 2015, A&A, 582, A81

Johnson, C. I., Rich, R. M., Kobayashi, C., & Fulbright, J. P. 2012, ApJ, 749, 175

Jönsson, H., Holtzman, J. A., Allende Prieto, C., et al. 2020, AJ, 160, 120

Jönsson, H., Ryde, N., Harper, G. M., Richter, M. J., & Hinkle, K. H. 2014, ApJ, 789, L41

Jönsson, H., Ryde, N., Nordlander, T., et al. 2017a, A&A, 598, A100

Jönsson, H., Ryde, N., Schultheis, M., & Zoccali, M. 2017b, A&A, 600, C2

Karakas, A. I. & Lattanzio, J. C. 2014, , 31, e030

Kobayashi, C., Karakas, A. I., & Lugaro, M. 2020, ApJ, 900, 179

Kormendy, J. & Kennicutt, Robert C., J. 2004, ARA&A, 42, 603

Korn, A. J., Grundahl, F., Richard, O., et al. 2007, ApJ, 671, 402

Kratz, K.-L., Farouqi, K., Pfeiffer, B., et al. 2007, ApJ, 662, 39

Lattanzio, J. C. 1989, ApJ, 344, L25

Lind, K., Korn, A. J., Barklem, P. S., & Grundahl, F. 2008, A&A, 490, 777

Liu, F., Asplund, M., Yong, D., et al. 2019, A&A, 627, A117

Lomaeva, M., Jönsson, H., Ryde, N., Schultheis, M., & Thorsbro, B. 2019, A&A, 625, A141

Madau, P. & Dickinson, M. 2014, ARA&A, 52, 415

Matrozis, E., Ryde, N., & Dupree, A. K. 2013, A&A, 559, A115

Matteucci, F. & Brocato, E. 1990, ApJ, 365, 539

Matteucci, F., Grisoni, V., Spitoni, E., et al. 2019, MNRAS, 487, 5363

Matteucci, F., Romano, D., Arcones, A., Korobkin, O., & Rosswog, S. 2014, MNRAS, 438, 2177

McMillan, P. J. 2018, Research Notes of the American Astronomical Society, 2, 51

McWilliam, A. 2016, Publications of the Astronomical Society of Australia, 33, e040

Mikolaitis, Š., de Laverny, P., Recio-Blanco, A., et al. 2017, A&A, 600, A22

Mishenina, T. V., Pignatari, M., Korotin, S. A., et al. 2013, A&A, 552, A128

Nordlander, T., Korn, A. J., Richard, O., & Lind, K. 2012, ApJ, 753, 48

Petit, P., Louge, T., Théado, S., et al. 2014, PASP, 126, 469

Piskunov, N. & Valenti, J. A. 2017, A&A, 597, A16

Prantzos, N., Abia, C., Limongi, M., Chieffi, A., & Cristallo, S. 2018, MNRAS, 476, 3432

Prialnik, D. 2000, An Introduction to the Theory of Stellar Structure and Evolution (Cambridge University Press)

Reddy, B. E., Lambert, D. L., & Allende Prieto, C. 2006, MNRAS, 367, 1329

Reddy, B. E., Tomkin, J., Lambert, D. L., & Allende Prieto, C. 2003, MNRAS, 340, 304

Rosswog, S., Korobkin, O., Arcones, A., Thielemann, F. K., & Piran, T. 2014, MNRAS, 439, 744

Rosswog, S., Liebendörfer, M., Thielemann, F. K., et al. 1999, A&A, 341, 499

Rosswog, S., Piran, T., & Nakar, E. 2013, MNRAS, 430, 2585

Ryde, N., Jönsson, H., Mace, G., et al. 2020, ApJ, 893, 37

Salpeter, E. E. 1955, ApJ, 121, 161

Scalo, J. M. 1986, , 11, 1

Shen, J. & Zheng, X.-W. 2020, Research in Astronomy and Astrophysics, 20, 159

Siegel, D. M., Barnes, J., & Metzger, B. D. 2018, arXiv:1810.00098

Sneden, C., Cowan, J. J., Ivans, I. I., et al. 2000, The Astrophysical Journal Letters, 533, L139

Souto, D., Allende Prieto, C., Cunha, K., et al. 2019, ApJ, 874, 97

Tanvir, N. R., Levan, A. J., González-Fernández, C., et al. 2017, ApJ, 848, L27

Telting, J. H., Avila, G., Buchhave, L., et al. 2014, Astronomische Nachrichten, 335, 41

Thielemann, F.-K., Arcones, A., Käppeli, R., et al. 2011, Progress in Particle and Nuclear Physics, 66, 346 , particle and Nuclear Astrophysics

Travaglio, C., Gallino, R., Arnone, E., et al. 2004, ApJ, 601, 864

Trippella, O., Busso, M., Maiorca, E., Käppeler, F., & Palmerini, S. 2014, ApJ, 787, 41

Valenti, J. A. & Piskunov, N. 1996, Astronomy and Astrophysics Supplement Series, 118, 595

Van der Swaelmen, M., Barbuy, B., Hill, V., et al. 2016, A&A, 586, A1

Wanajo, S., Janka, H.-T., & Müller, B. 2011, ApJ, 726, L15

Weinberg, D. H., Holtzman, J. A., Hasselquist, S., et al. 2019, ApJ, 874, 102

Zoccali, M., Hill, V., Lecureur, A., et al. 2008, A&A, 486, 177

A&A 631, A113 (2019)
https://doi.org/10.1051/0004-6361/201936343

Astronomy & Astrophysics

Abundances of disk and bulge giants from high-resolution optical spectra

IV. Zr, La, Ce, Eu⋆,⋆⋆

R. Forsberg[1], H. Jönsson[1,2], N. Ryde[1,3], and F. Matteucci[4,5,6]

[1] Lund Observatory, Department of Astronomy and Theoretical Physics, Lund University, Box 43, 221 00 Lund, Sweden
e-mail: rebecca@astro.lu.se
[2] Materials Science and Applied Mathematics, Malmö University, 205 06 Malmö, Sweden
[3] Université Côte d'Azur, Observatoire de la Côte d'Azur, CNRS, Laboratoire Lagrange, Bd de l'Observatoire, CS 34229, 06304 Nice Cedex 4, France
[4] Dipartimento di Fisica, Sezione di Astronomia, Università di Trieste, via G.B. Tiepolo 11, 34131 Trieste, Italy
[5] INAF – Osservatorio Astronomico di Trieste, via G.B. Tiepolo 11, 34131 Trieste, Italy
[6] INFN – Sezione di Trieste, via Valerio 2, 34134 Trieste, Italy

Received 18 July 2019 / Accepted 18 September 2019

ABSTRACT

Context. Observations of the Galactic bulge suggest that the disk formed through secular evolution rather than gas dissipation and/or mergers, as previously believed. This would imply very similar chemistry in the disk and bulge. Some elements, such as the α-elements, are well studied in the bulge, but others like the neutron-capture elements are much less well explored. Stellar mass and metallicity are factors that affect the neutron-capture process. Due to this, the enrichment of the ISM and the abundance of neutron-capture elements vary with time, making them suitable probes for Galactic chemical evolution.

Aims. In this work, we make a differential comparison of neutron-capture element abundances determined in the local disk(s) and the bulge, focusing on minimising possible systematic effects in the analysis, with the aim of finding possible differences/similarities between the populations.

Methods. Abundances are determined for Zr, La, Ce, and Eu in 45 bulge giants and 291 local disk giants, from high-resolution optical spectra. The abundances are determined by fitting synthetic spectra using the SME-code. The disk sample is separated into thin- and thick-disk components using a combination of abundances and kinematics.

Results. We find flat Zr, La, and Ce trends in the bulge, with a ~0.1 dex higher La abundance compared with the disk, possibly indicating a higher s-process contribution for La in the bulge. [Eu/Fe] decreases with increasing [Fe/H], with a plateau at around [Fe/H] ~ −0.4, pointing at similar enrichment to α-elements in all populations.

Conclusions. We find that the r-process dominated the neutron-capture production at early times both in the disks and bulge. Further, [La/Eu] ratios for the bulge are systematically higher than for the thick disk, pointing to either a) a different amount of SN II or b) a different contribution of the s-process in the two populations. Considering [(La+Ce)/Zr], the bulge and the thick disk follow each other closely, suggesting a similar ratio of high-to-low-mass asymptotic giant branch stars.

Key words. stars: abundances – Galaxy: bulge – solar neighborhood – Galaxy: evolution

1. Introduction

Our view of the structure and formation of the Galactic bulge has changed dramatically over the past decade. Earlier, the prevailing view was that the bulge is a spheroid in a disk formed in an early, rapid, dissipative collapse (e.g. Immeli et al. 2004), naturally resulting from major mergers for example, converting disks to classical bulges (e.g. Shen & Li 2016). However, with new findings and an accumulation of data, what we call the bulge is today predominately considered to be mainly the inner structures of the Galactic bar seen edge-on (e.g. Portail et al. 2017). The details of its structure and timescales for its formation are nevertheless unclear (e.g. Barbuy et al. 2018).

Metallicity distributions and abundance-ratio trends with metallicity provide important means to determine the evolution of stellar populations, also in the bulge. Trends of different element groups formed in different nucleosynthetic channels provide strong complementary constraints. Also, comparisons of trends between different stellar populations, for example the local thick disk, can be used to constrain the history of the bulge. Whether or not there is an actual difference in abundance trends with metallicity between the bulge and the local thick disk is unclear (McWilliam 2016; Barbuy et al. 2018; Zasowski et al. 2019; Lomaeva et al. 2019). Some elements such as Sc,

⋆ Full Tables A.1–A.4 are only available at the CDS via anonymous ftp to cdsarc.u-strasbg.fr (130.79.128.5) or via http://cdsarc.u-strasbg.fr/viz-bin/cat/J/A+A/631/A113

⋆⋆ Based on observations made with the Nordic Optical Telescope (programs 51-018 and 53-002) operated by the Nordic Optical Telescope Scientific Association at the Observatorio del Roque de los Muchachos, La Palma, Spain, of the Instituto de Astrofisica de Canarias, spectral data retrieved from PolarBase at Observatoire Midi Pyrénées, and observations collected at the European Southern Observatory, Chile (ESO programs 71.B-0617(A), 073.B-0074(A), and 085.B-0552(A)).

V, Cr, Co, Ni, and Cu show differences in some investigations, whereas others show great similarities. New abundance studies minimising systematic uncertainties are clearly needed.

An important nucleosynthetic channel that has not yet been thoroughly investigated in the bulge is that of the heavy elements, namely the neutron-capture elements. These can be divided into two groups: the slow (s)- and rapid (r)-process elements, depending on the timescales between the subsequent β-decay and that of the interacting neutron flux (Burbidge et al. 1957). The neutron flux in the s-process is such that the timescale of interaction is slower than the subsequent β-decay, making the elements created in this process stable and generally found in the so-called valley of stability, whilst it is the other way around for the r-process, resulting in the creation of heavier elements. As a point of reference, the s-process therefore produces the lighter elements after iron ($A \geq 60$), whereas the r-process is the dominating production process for the heaviest elements. Nonetheless, it is important to keep in mind that the production of heavier elements is a combination of the two processes and an "s- or r-process element" simply refers to an element with a dominating contribution from one of the processes. The neutron densities required for the s- and r-processes are $\leq 10^{7}-10^{15}$ cm^{-3} (Busso et al. 1999; Karakas & Lattanzio 2014) and somewhere between $10^{24}-10^{28}$ cm^{-3} (Kratz et al. 2007), respectively, putting some constraints on the astrophysical sites where they can occur.

The s-process can in turn be divided into three sub-processes: the weak, main and strong s-processes taking place in massive stars (weak) and asymptotic giant branch (AGB) stars (main, strong). Furthermore, the s-process elements can be divided into the light, heavy, and very heavy s-process elements, the naming originating from their atomic masses of A = 90, 138 and 208 (around Zr, La, and Pb, respectively). A build-up is created at these stable nuclei (N = 50, 82, and 126, also known as magic numbers) due to isotopes with low neutron cross sections, creating bottlenecks in the production of heavier elements and in turn, peaks of stable isotopes. Thus, the naming first-second-, and third-peak s-process is often also used for the light, heavy and very heavy s-process elements. In this work, light and heavy s-process elements produced in the main s-process will be analysed (Zr, La, Ce).

The main s-process takes place in the interior of low- and intermediate-mass AGB stars (Herwig 2005; Karakas & Lattanzio 2014) with the neutrons originating from the reactions ^{13}C$(\alpha, n)^{16}$O and ^{22}Ne$(\alpha, n)^{25}$Mg. The second reaction takes place at higher temperatures in AGB stars with initial masses of $>4\ M_{\odot}$. The process takes place in the so-called ^{13}C-pocket in between the hydrogen and helium burning shells during the third dredge-up (TDU; Bisterzo et al. 2017). Since AGB stars have an onset delay on cosmic scales, a non-negligible fraction of the s-process-dominated elements is likely to originate from the r-process at early times. Furthermore, the light s-process elements (first-peak s-process) can have a possible production from the weak s-process, taking place in helium core burning and in the subsequent convective carbon-burning-shell phase in massive stars (Couch et al. 1974). However, previous observations cannot fully explain the abundance of the light s-process elements at early times, and other possible origins have therefore been proposed (e.g. LEPP; Travaglio et al. 2004; Cristallo et al. 2015).

The production site(s) for r-process elements is yet to be constrained, but the proposed sites are various neutron-rich (violent) events, such as core-collapse supernovae (CC SNe), collapsars, and the mergers of heavy bodies in binaries, such as neutron star mergers (Sneden et al. 2000; Thielemann et al. 2011, 2017). The electromagnetic counterpart to the observed neutron merger GW170817 (Abbott et al. 2017) indeed showed r-process elements. Research is still ongoing to determine whether or not neutron star mergers are the only, or even the dominating, source of r-process elements (e.g. Thielemann et al. 2018; Côté et al. 2019; Siegel et al. 2019; Kajino et al. 2019).

In order to put constraints on the neutron capture yields, it is important to have reliable observational abundances to compare with the models. In the review paper on the chemical evolution of the bulge by McWilliam (2016), the necessity of having properly measured abundances for the disk in order to have a reference sample for bulge measurements is stressed, and these are provided in this work.

Regarding the determination of neutron-capture elements in bulge stars, such analyses have been made previously by Johnson et al. (2012), Van der Swaelmen et al. (2016), and Duong et al. (2019). Johnson et al. (2012) studied stars in Plaut's field ($b = -8°$) observed with the Hydra multifibre spectrograph at the Blanco 4m telescope, determining the abundances of Zr, La, Nd, and Eu. Their [La/Fe] trend versus metallicity of the stars in the bulge field is clearly different from that of the thick disk. These latter authors therefore concluded that the metal-poor bulge, or the inner disk, is likely chemically different from that of the thick disk. Van der Swaelmen et al. (2016) studied Ba, La, Ce, Nd and Eu in 56 Galactic bulge giants observed with FLAMES/UVES at the VLT, finding that the s-process elements Ba, La, Ce, and Nd have decreasing [Ba,La,Ce,Nd/Fe] abundances with increasing metallicity, separating them from the flatter thick-disk trends. Additionally, in the work by Duong et al. (2019), Zr, La, Ce, Nd and Eu are measured for a large bulge sample at latitudes of $b = -10°$, $-7.5°$ and $-5°$, observed with the HERMES spectrograph on the Anglo-Australian Telescope. These latter authors find indications of the bulge having a higher star formation rate than that of the disk.

Johnson et al. (2012) and Van der Swaelmen et al. (2016) compare their bulge abundances with previously determined disk abundances, mainly from dwarf stars, which might obstruct the interpretation of the comparative abundances due to the risk of systematic uncertainties between analyses of dwarf and giant stars[1]. Previous studies by Meléndez et al. (2008) and Gonzalez et al. (2015) stressed the importance of comparing stars within the same evolutionary stage. Furthermore, in investigations of atomic diffusion and mixing in stars (Korn et al. 2007; Lind et al. 2008; Nordlander et al. 2012; Gruyters et al. 2016; Souto et al. 2019; Liu et al. 2019), it has been shown that dwarf stars might have systematically lower elemental abundances compared to evolved stars, suggesting that abundances measured from dwarf stars are too low. The magnitude of this depletion is measurable and should, in general, be considered for the relevant elements in order to properly probe the Galactic composition and its evolution based on dwarf stars.

In this paper, we study the four neutron-capture elements Zr, La, Ce, and Eu determined from optical spectra of giants observed with FLAMES/UVES for the bulge sample. We compare the obtained abundance-ratio trends with that of the local disk obtained from a comparison sample of similarly analysed giants (observed with FIES at high resolution in the same wavelength range). Section 2 describe the bulge and disk samples. The same methodology for determining the stellar parameters

[1] Duong et al. (2019), to as large an extent as possible, use the same atomic data and analysis method in their work as their comparison sample, GALAH (Buder et al. 2018), to minimise systematic offsets.

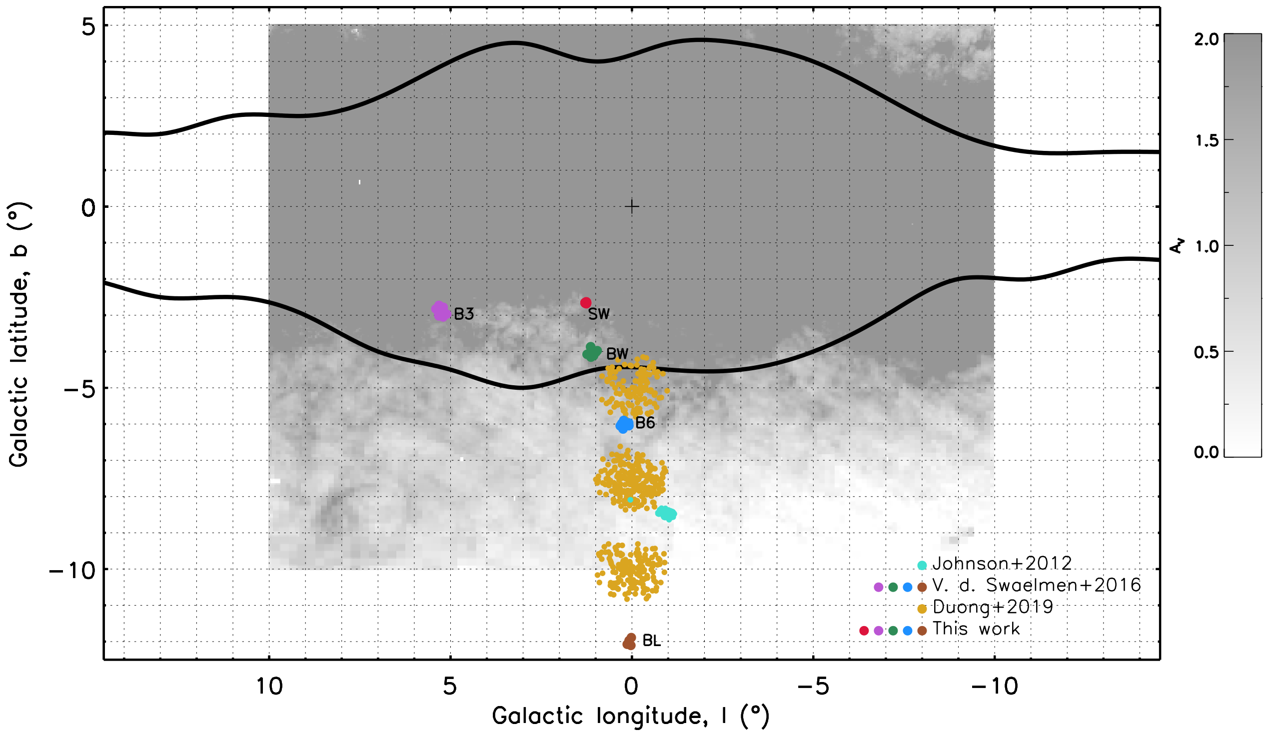

Fig. 1. Map of the Galactic bulge showing the five analysed fields (SW, B3, BW, B6, and BL). The bulge samples from Johnson et al. (2012), Van der Swaelmen et al. (2016), and Duong et al. (2019) are also marked in the figure. The dust extinction towards the bulge is taken from Gonzalez et al. (2011, 2012) and scaled to optical extinction (Cardelli et al. 1989). The scale saturates at $A_V = 2$, which is the upper limit in the figure. The COBE/DIRBE contours of the Galactic bulge, in black, are from Weiland et al. (1994).

and abundances (a carefully chosen set of spectral lines) ensures a minimisation of the systematic uncertainties in the comparison of the two samples, following the same methodology as the previous papers in this series; Jönsson et al. (2017a,b); Lomaeva et al. (2019), see Sect. 3. We present the results in Sect. 4 and discuss these in Sect. 5.

2. Observations

2.1. Bulge sample

Since large amounts of dust lies in the line of sight towards the Galactic centre resulting in a high optical extinction, observing bulge stars can be challenging at optical wavelengths. Our ambition was to include fields as close to the centre of the bulge as possible, whilst keeping to regions where the extinction is manageable.

The Galactic bulge sample consists of 45 giants (see Table A.1). The spectra were obtained using the spectrometer FLAMES/UVES mounted on the VLT, Chile, observed in May-August 2003-2004. Twenty-seven of these spectra were also analysed in Van der Swaelmen et al. (2016). In addition to these, 18 spectra from the Sagittarius Window, $(l, b) = (1.29°, -2.65°)$, lying closer to the Galactic plane in a region with relatively low extinction, are added to the sample analysed here. These were observed in August 2011 (ESO programme 085.B-0552(A)). In total, five bulge fields are included in the bulge sample: SW (the Sagittarius Window), BW (Baade's Window), BL (the Blanco field), B3, and B6[2]. The fields can be seen in Fig. 1, overlaid on an optical extinction map, together with the fields analysed in Johnson et al. (2012) and Duong et al. (2019). From Fig. 1 one can see that the SW field lies in a region of relatively low extinction and closer to the Galactic plane than the other fields.

The FLAMES/UVES instrument allows for simultaneous observation of up to seven stars. Depending on the extinction and local conditions, each setting in our observations required an integration time of somewhere between 5 and 12 h. The achieved signal-to-noise ratios (S/N) of the recorded bulge spectra are between 10 and 80. The resolving power of the spectra is $R \sim 47\,000$ and the usable wavelength coverage is limited to the range 5800–6800 Å.

The distances to our bulge stars are estimated to range between 4 and 12 kpc from the solar system (Bailer-Jones et al. 2018), placing the stars within the Galactic regions classified as the bulge by Wegg et al. (2015). Although it should be noted that distance estimation can be rather troublesome and *Gaia* DR2 (Gaia Collaboration 2016, 2018) reports a parallax uncertainty higher than 20% for the majority of our bulge stars.

2.2. Disk sample

The disk sample consists of 291 giants stars, a majority of these placed within 2 kpc of the solar system (see Table A.2). The bulk of the sample is observed at the Nordic Optical Telescope (NOT), La Palma, using the FIbre-fed Echelle Spectrograph (FIES; Telting et al. 2014), under the programme 51-018 (150 stars) in May–June 2015 and 53-002 (63 stars) in June 2016. Forty-one spectra were taken from the stellar sample in Thygesen et al. (2012), also observed using the FIES at the NOT. An additional 18 spectra were downloaded from the FIES archive. Lastly, 19

[2] The naming of the fields follows the convention seen in Lecureur et al. (2007).

spectra were taken from the PolarBase data base (Petit et al. 2014) where NARVAL and ESPaDOnS were used (mounted on Telescope *Bernard Lyot* and Canada–France–Hawaii Telescope, respectively). The FIES and PolarBase have similar resolving powers of $R \sim 67\,000$ and $R \sim 65\,000$, respectively.

All three spectrometers cover wide regions in the optical domain, but in order to maximise the coherency in this work, the wavelength region used is restricted to that of the bulge spectra: 5800–6800 Å. The resulting S/N of the FIES spectra are around 80–120 per data point in the reduced spectrum. Similar values can be found for the PolarBase spectra whereas the Thygesen et al. (2012) spectra have a lower S/N of about 30–50. Details of how the S/N was calculated can be found in Jönsson et al. (2017a).

The reduction of the FIES spectra was preformed using the standard FIES pipeline and the Thygesen et al. (2012) and PolarBase data was already reduced. A crude normalisation of all spectra was done initially with the IRAF task `continuum`. Later in the analysis, the continuum is re-normalised more carefully by a manual placement of continuum regions and subsequently fitting a straight line to these, allowing a higher precision of the abundance determination (more on this in Sect. 3.3).

Telluric lines have not been removed from the spectra. Instead a telluric spectrum from the Arcturus atlas (Hinkle et al. 2000) has been plotted over the appropriately shifted observed spectra and affected regions have been avoided on a star-by-star basis.

3. Analysis

The analysis of the spectra and the determination of the stellar abundances follows the same methodology as described in the previous papers in this series: Jönsson et al. (2017a,b) and Lomaeva et al. (2019). This section describes the general methodology as well as the specific details relevant for this work.

3.1. General methodology

To determine the stellar abundances, synthetic spectra are modelled using the tool Spectroscopy Made Easy (SME, Valenti & Piskunov 1996; Piskunov & Valenti 2017). For a given set of stellar parameters ($T_{\rm eff}$, $\log g$, [Fe/H], and microturbulence, $\xi_{\rm micro}$), SME interpolates in a grid of pre-calculated model atmospheres and calculates a synthetic spectrum of a region of choice. By defining line and continuum masks over spectral regions of interest, SME can simultaneously fit, using χ^2-minimisation (Marquardt 1963), both stellar photospheric parameters and/or stellar abundances. Figure 2 shows the line definitions and continuum placements for the bulge star B6-F1 and the spectral lines used in the analysis.

The stellar parameters of the stars analysed are determined as described in Sect. 3.2 below. Metallicity-scaled solar abundances (Grevesse et al. 2007) are assumed in SME, except for the α-elements that have already been determined in Jönsson et al. (2017b).

Spectroscopy Made Easy uses a grid of MARCS models[3] (Gustafsson et al. 2008) that adopts spherical symmetry for $\log g < 3.5$, which is the case for the majority of our stars, but otherwise adopts plane parallel symmetry. Some non-local thermodynamic equilibrium (NLTE) effects have been reported for the elements analysed here: Zr is shown by Velichko et al. (2010) to be weakly dependent on temperature; and Mashonkina & Gehren (2000) find that they need small NLTE corrections

[3] Available at `marcs.astro.uu.se`

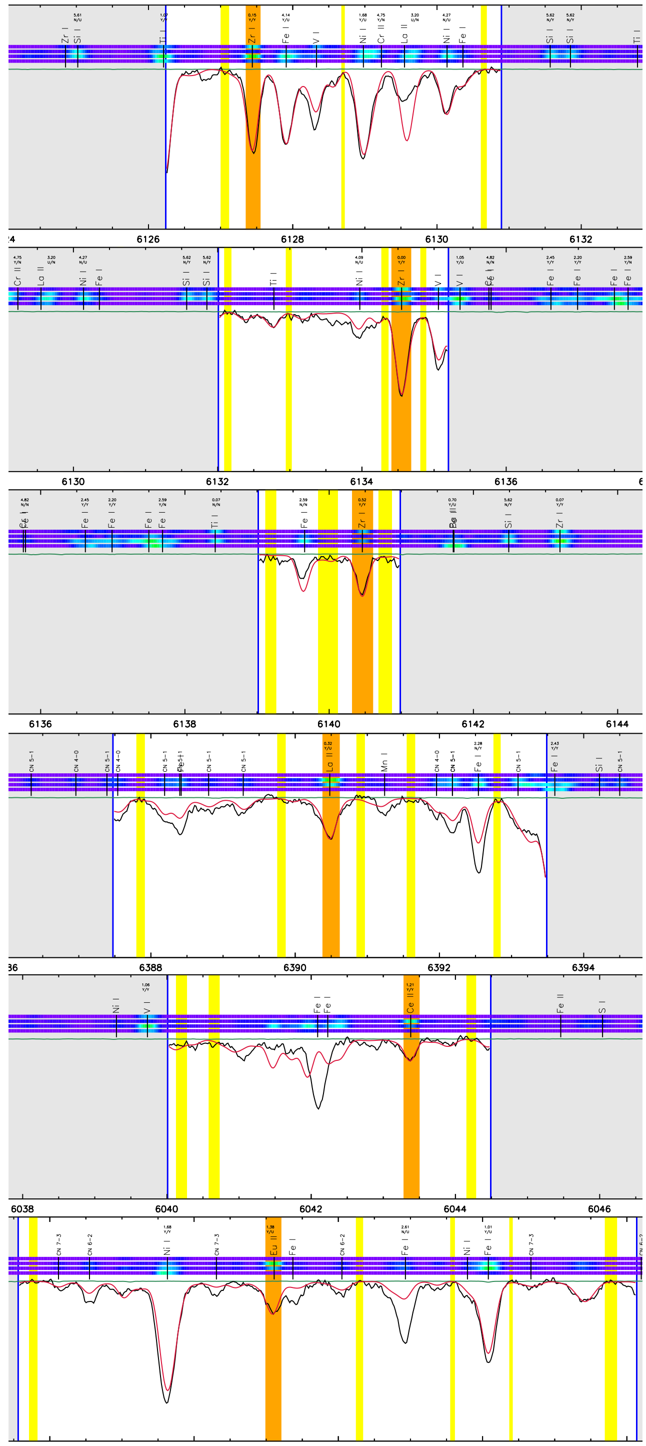

Fig. 2. Observed spectrum (black) of the bulge star B6-F1 ($S/N = 54$). The lines for abundance determination of Zr (three lines), La, Ce, and Eu (one line each) are marked out as the orange regions. The yellow regions are the manually placed continuum and the red spectrum is the synthetic one. The segments within which the synthetic spectrum is modelled are marked as the white wavelength regions between the blue vertical lines in each panel. The four horizontal lines above each spectrum indicate the lines' sensitivity in the stellar parameters $T_{\rm eff}$, $\log g$, [Fe/H] and $\xi_{\rm micro}$, respectively, where green is more sensitive than blue.

of the order of +0.03 dex for Eu in their analysis of cool dwarfs. Nonetheless, the analysis in this work is done under the assumption of LTE.

3.2. Stellar parameters

The stellar parameters used are determined in Jönsson et al. (2017a,b) (where a more detailed description can be found) by fitting synthetic spectra for unsaturated and unblended Fe I and Fe II lines, Ca I lines, and $\log g$ sensitive Ca I line wings, while $T_{\rm eff}$, $\log g$, [Fe/H], $\xi_{\rm micro}$, and [Ca/Fe] were set as free parameters in SME. The Fe I line has NLTE corrections adopted from Lind et al. (2012). The reported uncertainties for these parameters in Jönsson et al. (2017a,b) for a typical disk star of $S/N \sim 100$ are $T_{\rm eff}$ ±50 K, $\log g$ ± 0.15 dex, [Fe/H] ± 0.05 dex, and ±0.1 km s^{-1} for $\xi_{\rm micro}$. For a typical bulge star, the S/N is significantly lower (median of 38), and hence the uncertainties greater; $T_{\rm eff}$ ± 100 K, $\log g \pm 0.30$ dex, [Fe/H] ± 0.10 dex and $\xi_{\rm micro} \pm 0.2$ km s^{-1}. These values are later used in the uncertainties estimations; see Sect. 4.2.

3.3. Abundance determination

The atomic line data used for the abundance determination are collected from the *Gaia*-ESO line list version 6 (Heiter et al. 2015, and in prep.). From here we get wavelengths, excitation energies, and transition probabilities (as well as broadening parameters, when existing). The transition probabilities for the elements investigated here, Zr, La, Ce, and Eu, come from Biemont et al. (1981), Lawler et al. (2001a), Lawler et al. (2009), and Lawler et al. (2001b), respectively. All available lines for these elements in the given wavelength region (5800–6800 Å) were investigated individually in order to exclude lines that could not be modelled properly (due to blends, bad atomic data, or other systematics). As for Zr, where three separate lines were suitable for abundance determination, the lines were ultimately fitted simultaneously. Finally, the determined SME abundances were, in the post-process, re-normalised to the most up-to-date solar values provided by Grevesse et al. (2015). The final set of lines used for abundance determination is presented in Table 1. Apart from the atomic lines, we include the molecules C_2 (Brooke et al. 2013) and CN (Sneden et al. 2014) in the synthesis.

For La and Eu, hyperfine splitting (hfs) had to be taken into account. By not taking hfs into account there is a risk of overestimating the measured abundance (Prochaska & McWilliam 2000; Thorsbro et al. 2018). Additionally, isotopic shift (IS) has to be considered for Zr, Ce, and Eu. The shift is caused by the isotopes having shifted energy levels, resulting in radiative transitions with shifted wavelengths. Isotopic shift is included by manually identifying the set of transitions for each isotope in the line list and scaling the $\log(gf)$ to the relative solar isotopic abundances; see Table 2.

3.4. Population separation

The classification of the stellar populations in the disk (thin/thick) can be done in several ways, namely by kinematics, age, geometry, and chemistry. Even so, the separation of these two components is somewhat debated and the transition between them might be a gradient rather than a clear separation. The results by Hayden et al. (2015) show that the scale length of the thin disk extends further out than that of the thick disk. The thick disk has been shown to be enriched in α-elements compared to that of the thin disk, in addition to thick disk stars having higher total velocities but slower rotational velocities (Bensby et al. 2014).

In Lomaeva et al. (2019) the separation into the two populations is computed for our disk sample, using a combination of stellar metallicity, abundances ([Ti/Fe] as determined in Jönsson et al. 2017b) and kinematics. The radial velocities from Table A.2, proper motions from *Gaia* DR2 (Gaia Collaboration 2016, 2018) and distances from McMillan (2018) are used to calculate the total velocities[4]. In total, kinematic data were available for 268 stars in the disk sample. The clustering method `Gaussian Mixture Model` (GMM), obtained from the `scikit-learn` module for Python (Pedregosa et al. 2011), is used to cluster the disk data into the two components. We refer to Lomaeva et al. (2019) for more details.

Table 1. Atomic lines used in the analysis.

Element	Wavelength [Å]	$\log(gf)$	$\chi_{\rm exc}^{\rm low}$ [eV]
Zr I	6127.440	−1.06	0.15
Zr I	6134.550	−1.28	0.00
Zr I	6140.460	−1.41	0.51
La II	6390.457	−2.01	0.32
La II	6390.469	−2.08	0.32
La II	6390.486	−1.90	0.32
La II	6390.501	−2.08	0.32
Ce II	6043.373	−0.48	1.21
Eu II	6645.057	−0.84	1.38
Eu II	6645.060	−0.78	1.38
Eu II	6645.068	−2.13	1.38
Eu II	6645.074	−0.84	1.38
Eu II	6645.083	−0.91	1.38
Eu II	6645.086	−0.90	1.38
Eu II	6645.098	−0.60	1.38
Eu II	6645.101	−0.95	1.38
Eu II	6645.121	−1.01	1.38
Eu II	6645.137	−1.09	1.38
Eu II	6645.149	−1.19	1.38

Notes. The elements and ionisation stages are given in Col. 1, the transition wavelengths in Col. 2, and the $\log(gf)$ values are listed in Col. 3. The excitation energies of the transitions lower level are given in Col. 4. **References.** The $\log(gf)$ data included in the *Gaia*-ESO line lists comes from Biemont et al. (1981) (Zr), Lawler et al. (2001a) (La), Lawler et al. (2009) (Ce) and Lawler et al. (2001b) (Eu).

Table 2. Isotope information of the elements.

Element(Z)	Baryon number	Relative abundance	Reference
Zr(40)	90:91:92:94:96	51:11:17:17:3	Nomura et al. (1983)
La(57)	139	100	de Laeter & Bukilic (2005)
Ce(58)	140:142	88:11	Chang et al. (1995)
Eu(63)	151:153	48:52	Chang et al. (1994)

Notes. Column 2 gives the baryon number of the stable isotopes that contribute to at least 1% to the solar system abundance. Column 3 gives the corresponding relative isotopic abundances of the stable isotopes as measured in the Sun, with references in the last column.

[4] $V_{\rm tot}^2 = U^2 + V^2 + W^2$.

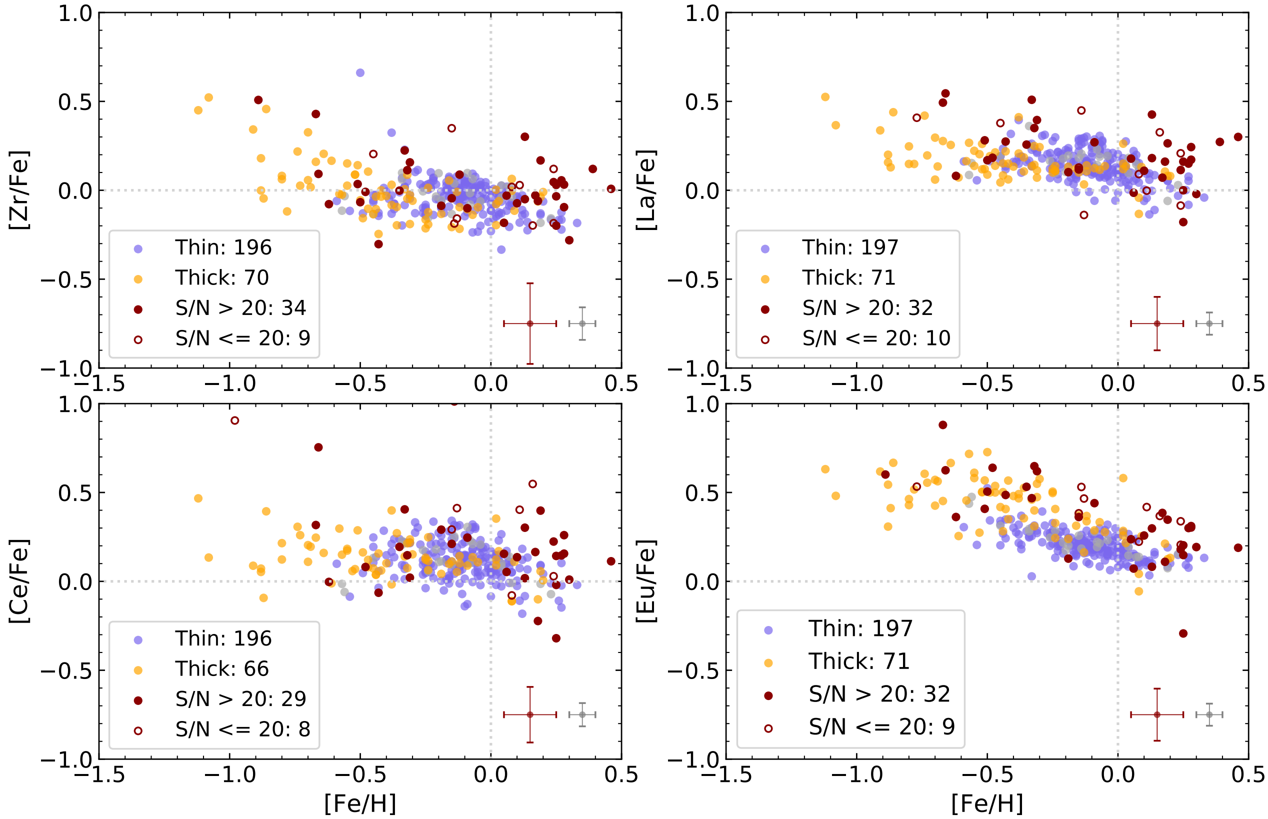

Fig. 3. Abundance ratio trends with metallicity, [X/Fe] against [Fe/H], for the thin- (blue) and thick-disk (yellow) stars as well as the bulge stars (red). Since it was not possible to determine all abundances in all spectra, the number of stars in each sample is included in the legend. Filled dark red circles indicate bulge stars with a S/N above 20, whereas the hollow red circles indicate a S/N equal to or less than 20. Some of the disk stars could not be classified as thick or thin disk stars; these are marked as grey dots. The typical uncertainty for the disk and the bulge sample, as described in Sect. 4.2, is marked in the lower right corner of every plot.

4. Results

4.1. Abundances

Our derived abundance ratios, [X/Fe], for Zr, La, Ce, and Eu, are plotted against [Fe/H] in Fig. 3. The population separation is applied to the disk sample and the number of stars in each population for which we could determine the abundance in question is noted in every panel. The bulge sample is plotted on top of the disk trends, where for the bulge we differentiate between spectra of high and low S/N, with a separation of $S/N = 20$. The typical uncertainties are noted in the plots, and the estimation of these is described in Sect. 4.2.

4.2. Uncertainties

Systematic errors generally originate from incorrectly determined stellar parameters, model atmosphere assumptions, continuum placement, and atomic data. This makes these errors hard to estimate. To get a sense of the systematic uncertainties, one can compare to reference stars. In Jönsson et al. (2017a) they compare the determined stellar parameters to those of three overlapping *Gaia* benchmark stars determined in Jofré et al. (2015) and find that these are within the uncertainties of the *Gaia* benchmark parameters.

All spectra are analysed using the same line and continuum masks as well as the same atomic data, minimising possible random uncertainties. Therefore, the random uncertainties are to primarily be found in the (random) uncertainties of the stellar parameters. An approach to estimate the random uncertainties due to changes in the stellar parameters, is to analyse a typical spectrum several times using parameters that all vary within given distributions. The same method for estimating the uncertainties was used in Lomaeva et al. (2019).

Using the FIES spectrum of the standard star Arcturus[5], uncertainties were added to its initial stellar parameters, meaning that the stellar parameters were changed simultaneously, for a set of 500 runs with modified stellar parameters. A Gaussian distribution is used to generate the uncertainties, using the reported stellar parameter uncertainties as standard deviation (see Sect. 3.2). In the uncertainty estimation of the bulge abundances, we have not degraded the FIES Arcturus spectrum (with a resolution of 67 000) to match that of the bulge spectra (R of 47 000), but separate tests have shown this slightly lower resolution to have a negligible effect on the determined abundance.

The abundance uncertainties coming from the uncertainties in the stellar parameters are then calculated as

$$\sigma A_{\text{parameters}} = \sqrt{|\delta A_{T_{\text{eff}}}|^2 + |\delta A_{\log g}|^2 + |\delta A_{[\text{Fe/H}]}|^2 + |\delta A_{v_{\text{micro}}}|^2}, \quad (1)$$

[5] The giant star Arcturus (also known as α-Boo or HIP69673) has been analysed extensively due to its brightness, being the fourth brightest in the night sky, and is suitable as a reference of a typical giant star.

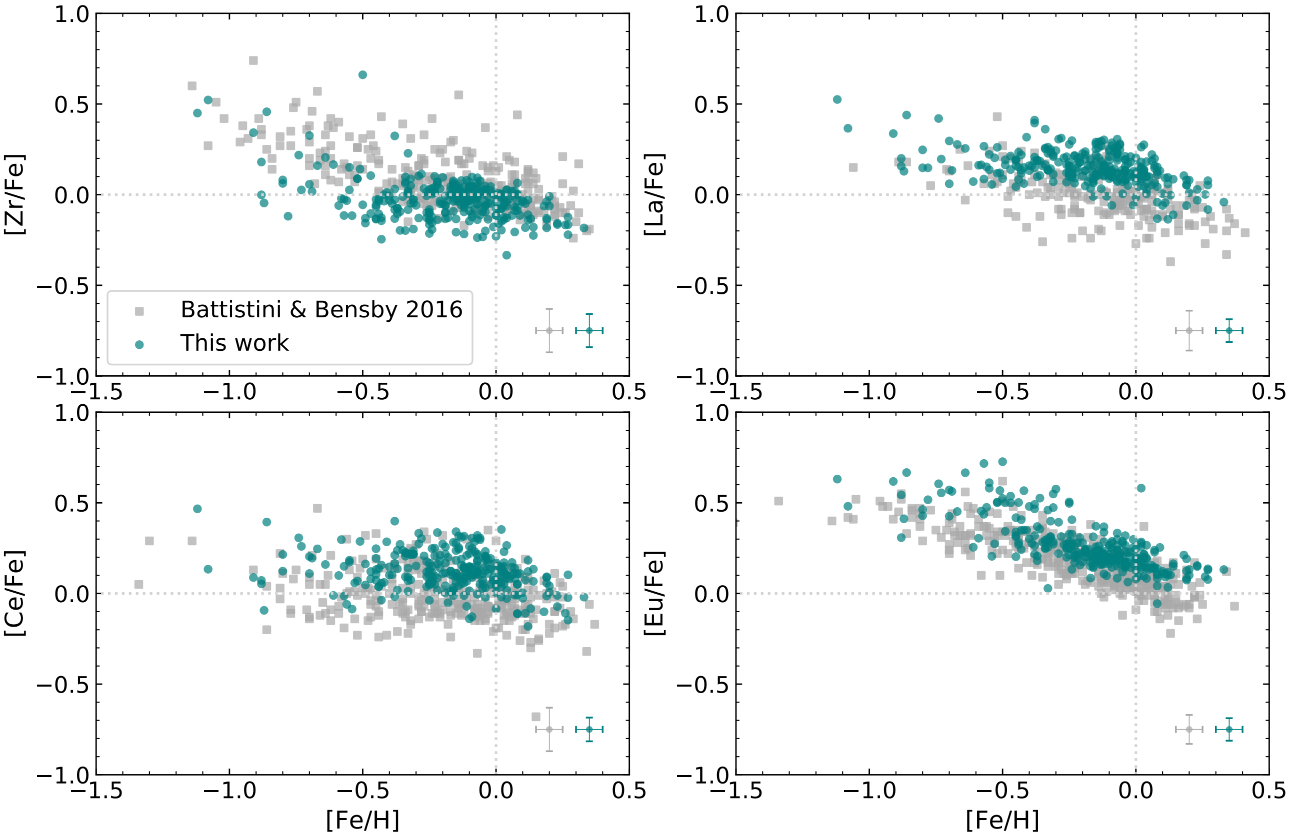

Fig. 4. Determined disk abundances in this work (teal) compared with the determined abundances from Battistini & Bensby (2016) (grey). The typical uncertainties for both data sets are indicated in the lower right corner of every plot, where the uncertainties are taken from Table 6 in Battistini & Bensby (2016).

Table 3. Estimated typical uncertainties for the disk and bulge sample using a generated set of stellar parameters for the giant star α-Boo.

$\sigma A_{\text{parameters}}$	Zr	La	Ce	Eu
Disk [dex]	0.09	0.06	0.07	0.06
Bulge [dex]	0.23	0.15	0.16	0.15

where, for non-symmetrical abundance changes, the mean value is used in the squared sums. The resulting uncertainties can be seen in Table 3.

5. Discussion

In this section we elaborate on the results. Firstly, we compare our separate abundance trends for the disks and bulge with previous literature studies in Sect. 5.1. Secondly, and this is the core of this investigation, in Sect. 5.2 we consider a more in-depth comparative analysis between our abundances for the bulge and disks populations, both determined in the same way. This is done to minimise the systematic uncertainties as much as possible. We then proceed in considering and discussing comparative abundance ratios such as [Eu/Mg], [Eu/La], and [second-peak s/first-peak s], also in Sect. 5.2 as well as Sect. 5.3.

To highlight features of the trend-plots, the running means of the samples are calculated and plotted (with a 1σ scatter). The number of data points in the running window is set to roughly 15% of the sample sizes (thin disk, thick disk, bulge). As a result, the running mean (and scatter) does not cover the whole trend range. For the bulge sample, only data points with *S/N* > 20 are included in the running mean. Henceforth, the running mean-trend is the one referred to when describing [X/Fe] or [X/Y] ratios (except for Sect. 5.1.1).

5.1. Comparison with selected literature trends

5.1.1. Disk sample

In Fig. 4 we compare our determined disk abundances with those determined for dwarf stars in the disk by Battistini & Bensby (2016). In general, the trends are similar for all elements, as well as the scatter in the determined abundance. The abundances of [La, Ce, Eu/Fe] seem to be systematically higher than those of Battistini & Bensby (2016) whereas the [Zr/Fe]-abundances appear to be slightly lower. The typical abundance uncertainties for Battistini & Bensby (2016) are 0.12, 0.11, 0.12, and 0.08 dex for Zr, La, Ce, and Eu, respectively (their Table 6), which is somewhat higher than ours (see Table 3). The possible shifts in the abundances could be due to systematic differences in dwarf and giant stars or in differing atomic data such as using different lines in the abundance determination. Indeed, there is no overlap in the atomic lines used in these two data sets, except for the La line at 6390 Å, although Battistini & Bensby (2016) use three additional lines for the La abundance determination.

Zirconium is a first-peak s-process element whereas La and Ce are second-peak s-process elements. [Zr,La/Fe] have

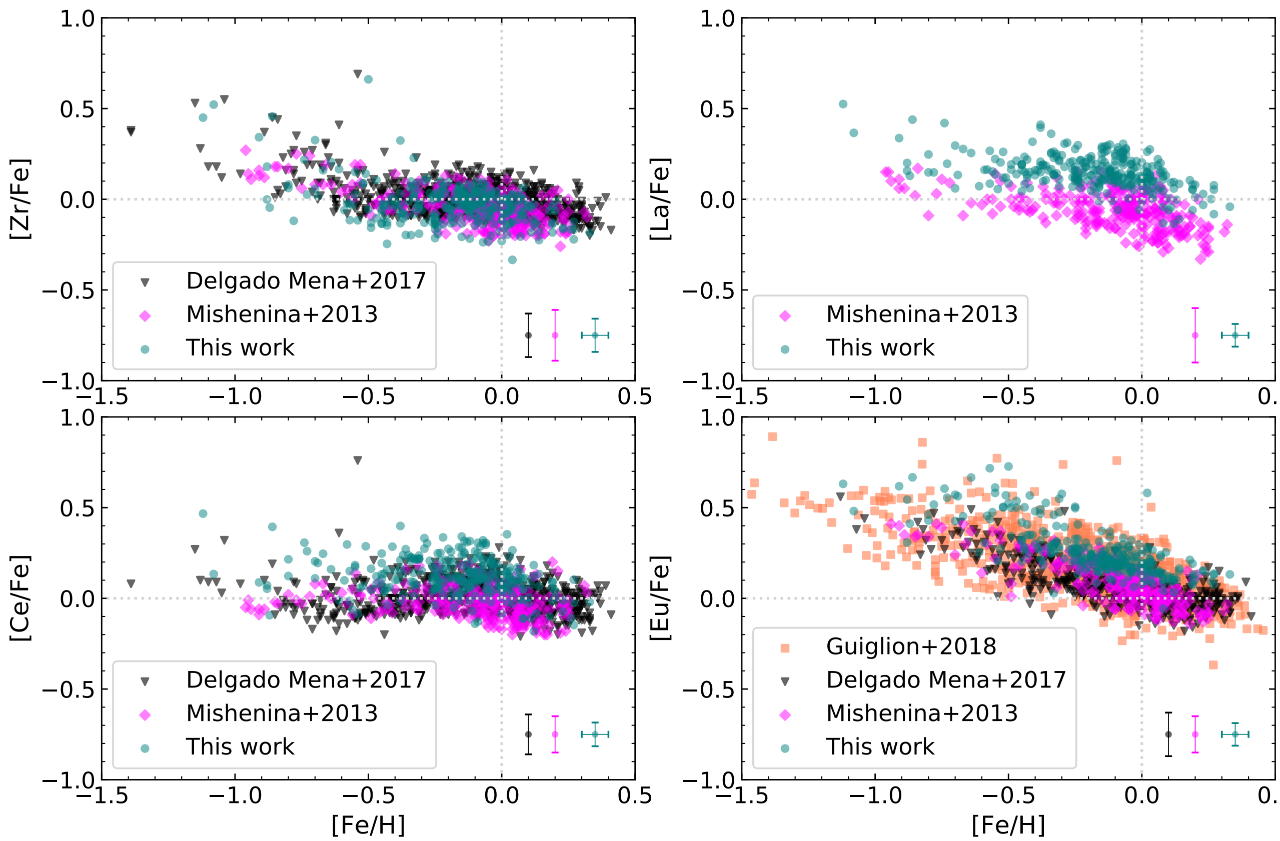

Fig. 5. Determined disk abundances in this work (teal) compared with selected literature trends: Mishenina et al. (2013) (pink), Delgado Mena et al. (2017) (black), and Guiglion et al. (2018) (orange). The typical uncertainties, when available, are indicated in the lower right corner of every plot, where the uncertainties from Mishenina et al. (2013) and Delgado Mena et al. (2017) (their Tables 3 and 4, respectively) are for a low T_{eff} star.

somewhat decreasing abundances with increasing metallicities, with a flattening of abundances for [Fe/H] above approximately −0.4. The [Ce/Fe] trend is flatter than [Zr/Fe] and [La/Fe], explained by the higher s-process contribution in the Ce production (66, 76 and 84% s-process contribution for Zr, La and Ce, respectively Bisterzo et al. 2014).

The scatter for the [La/Fe] abundances is higher, ~0.5 dex, over the metallicity range [−0.2, 0], compared to the rest of the metallicity domain with ~0.3 dex. This indicates that AGB stars produce the bulk of their s-elements through the main s-process. The increase in scatter can most likely be explained by the mass range of AGB stars, which enables (1) stars to produce s-process elements at different metallicities (times) as well as (2) different amounts of production of the first-/second-peak s-process for AGB stars with different masses (see Sect. 5.3). The increasing abundances when [Fe/H] is below −0.5 for the s-process elements Zr and La point at a production by the r-process at early times (see [Eu/Fe]). In addition to Battistini & Bensby (2016), our results are comparable to those reported in Mishenina et al. (2013) (Zr, La, Ce, Eu) and Delgado Mena et al. (2017) (Zr, Ce, Eu), on dwarf stars in the local disk; see Fig. 5. The typical uncertainties from Mishenina et al. (2013) and Delgado Mena et al. (2017) are chosen from their estimates of low T_{eff} stars; see their Tables 3 and 4, respectively.

For Eu, the trend decreases with increasing metallicity throughout our metallicity range, except for a plateau around [Fe/H] < −0.6. Europium has a reported r-process contribution of 94% (Bisterzo et al. 2014) and the observed trend indicates that the r-process has a continuous enrichment in the Galaxy, similar to that of the α-elements. Our Eu abundances compare well with those of Guiglion et al. (2018), including some subgiant and giant stars in their sample; see Fig. 5. We note that our measurements, and those of Battistini & Bensby (2016) and Guiglion et al. (2018), show, on average, slightly supersolar [Eu/Fe] abundances at solar metallicities, which is not seen in either Mishenina et al. (2013) or Delgado Mena et al. (2017). Of all the trends, ours is systematically high, not passing through the solar value at any metallicities.

5.1.2. Bulge sample

In Fig. 6 we compare our bulge trend with those observed in Johnson et al. (2012), Van der Swaelmen et al. (2016), and Duong et al. (2019). Twenty-seven of our stars and their spectra overlap with those of Van der Swaelmen et al. (2016), and the same spectral lines are used for the abundance determination. Nonetheless, we observe different trends as well as measure Zr in these stars.

Zirconium. In general, our [Zr/Fe] trend with metallicity is flat, with an increase at lower metallicities [Fe/H] < −0.5. It should be noted that the running mean is rather poorly defined at the edges and the feature is based primarily on the two most metal-poor stars in Fig. 3. Our trend agrees well with that of Johnson et al. (2012) within our overlapping metallicity ranges, whereas Duong et al. (2019) has overall decreasing abundances with increasing metallicities. Above [Fe/H] ~ 0.1, our [Zr/Fe]

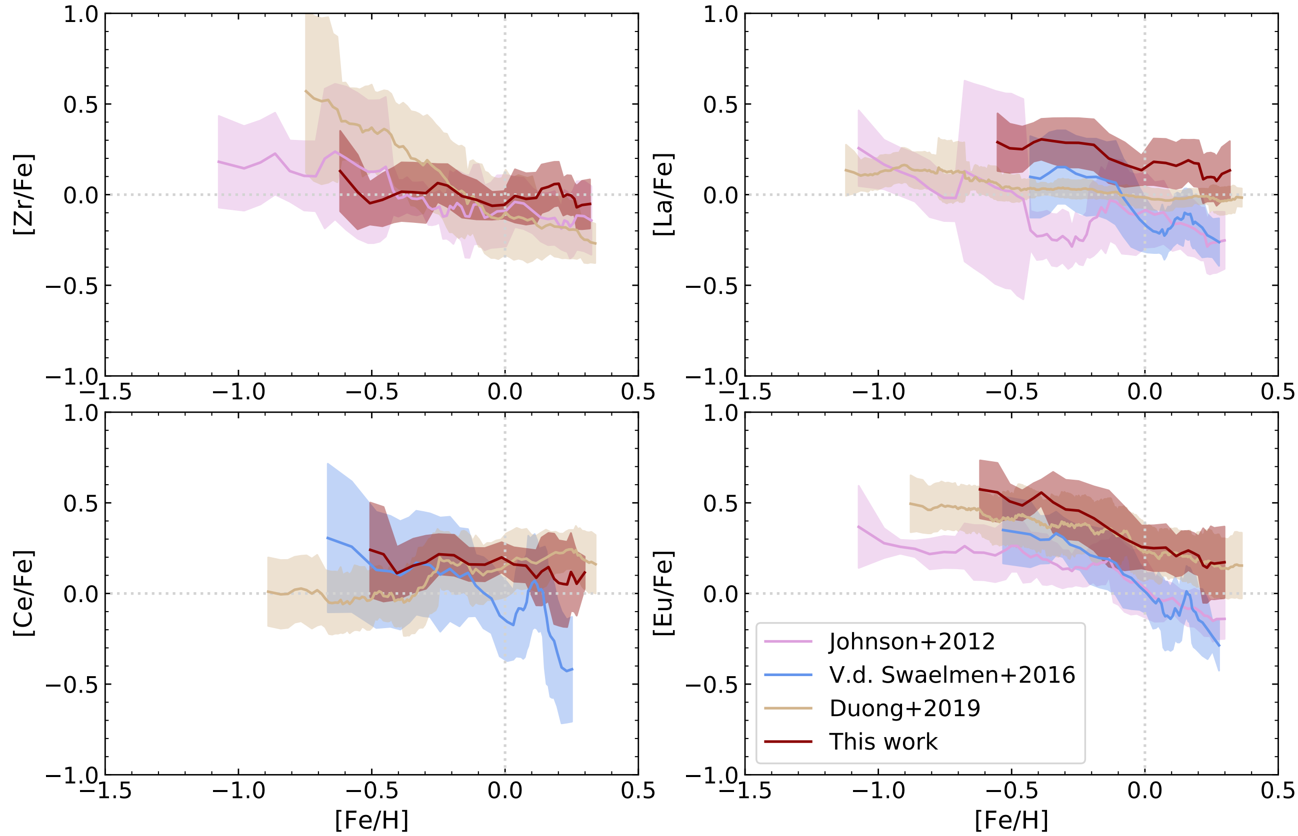

Fig. 6. Running mean for the bulge abundances determined in this work (red solid line) compared with the calculated running mean based on the abundances in Johnson et al. (2012) (pink solid line),Van der Swaelmen et al. (2016) (blue solid line), and Duong et al. (2019) (beige solid line), with a 1σ scatter (shaded regions, same colours as solid lines).

is solar while Johnson et al. (2012) and Duong et al. (2019) have subsolar [Zr/Fe], ours pointing at a higher s-process contribution in the production of Zr.

Lanthanum. Johnson et al. (2012) reports a dip in [La/Fe] abundance around [Fe/H] ~ −0.4 which is not observed in either of the other studies, or ours. Both Johnson et al. (2012) and Van der Swaelmen et al. (2016) produce decreasing [La/Fe] abundances with increasing metallicities, whilst both ours and that of Duong et al. (2019) exhibit only a very small decrease of [La/Fe] with increasing [Fe/H]. In general, our [La/Fe] abundances are higher than the other studies, which possibly could point at a higher s-process production in the bulge compared to previous work. However, we note that our bulge abundances, similarly to the disk abundances, are expected to suffer from a systematic offset in the determined [La/Fe] abundance ratios, preventing us from making a firm claim.

Cerium. Our [Ce/Fe] trend is flat throughout our metallicity range. Duong et al. (2019) also find a flat trend at solar scaled values, but with a slight step-wise increase at [Fe/H] ~ −0.3, thereafter following our trend. Van der Swaelmen et al. (2016) find a different [Ce/Fe] trend with decreasing [Ce/Fe] values with increasing metallicities.

Europium. All the published [Eu/Fe] bulge trends and ours decrease with increasing metallicity, although with slightly different slopes and different offsets. The Johnson et al. (2012) study covers the lowest metallicities of all the samples. The trend of Duong et al. (2019) and ours trace each other closely with super-solar abundances at all metallicities. The Johnson et al. (2012) and Van der Swaelmen et al. (2016) trends follow each other well in their overlapping metallicity region, with subsolar abundances above solar metallicities. There is an observable "knee" in the trend around [Fe/H] ~ −0.4, seen in all four studies mentioned above. Similarly to [La/Fe], our [Eu/Fe] abundances are higher than those in previous studies, although due to the possible systematic offsets we cannot draw any firm conclusions from this. However, since the main purpose of this work is to make a differential analysis between the disk and bulge abundances in this work, the possible systematic offset in our analysis is of less importance.

5.2. Disk and bulge comparison of the current study

In this section we compare our abundance-ratio trends, that is [X/Fe], for the bulge, the thin disk, and the thick disk as a function of the metallicity for the s-process elements Zr, La, and Ce, and the r-process element Eu. In Fig. 7 we directly compare the bulge population trends with those of the thin and the thick disk populations, determined in the same way in the present study.

The bulge and the disks have very similarly shaped s-process element trends (Zr, La, Ce). The bulge trend of [La/Fe] is slightly higher overall, especially at subsolar metallicities where [La/Fe] is ~0.1 dex higher than for the disk. We note that this is the opposite to findings in Duong et al. (2019). The metallicities of

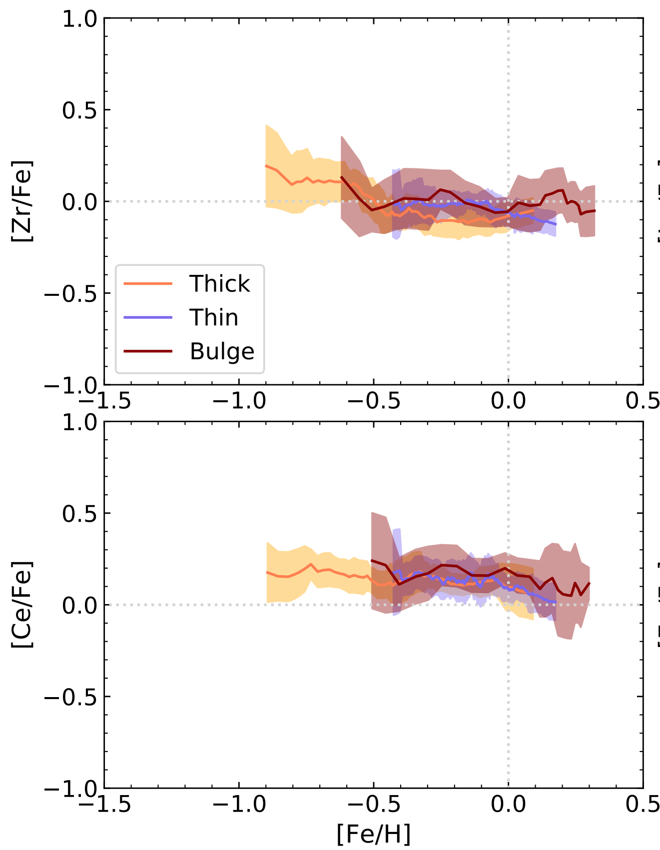

Fig. 7. Running mean for the bulge (red solid line) compared with the running mean of the thick disk (yellow solid line) and thin disk (blue solid line), with a 1σ scatter (shaded regions, same colours as solid lines).

the bulge sample extend to slightly higher values, pointing at a higher star formation rate of the bulge. Additionally, Matteucci et al. (2019) shows that implementing a Salpeter like initial mass function (IMF), which favours massive stars compared to typical IMFs for the disk, better reproduce bulge abundances.

For [Eu/Fe], the thick disk is enhanced as compared with the thin disk, reminding us of an α-element. The decreasing trend for metallicities larger than [Fe/H] $\gtrsim -0.4$ is a result of iron production by SN Ia after a time delay of roughly 100 Myr-1 Gyr (Matteucci & Brocato 1990; Ballero et al. 2007). The bulge traces the thick disk in the [Eu/Fe] abundance, suggesting the bulge has a similar star formation rate as that of the thick disk. A plateau, or a knee, can be seen around metallicities of approximately −0.4 for both the thick disk and the bulge. A knee at higher metallicities than in the solar vicinity was already predicted for the bulge by Matteucci & Brocato (1990) and in general for systems with higher star formation rates than in the solar vicinity.

In Fig. 8 we compare Eu with the well-determined α-element magnesium (from Jönsson et al. 2017b), by plotting [Eu/Mg], for the same stars. The resulting, mostly flat trend of all populations is already expected from the [Eu/Fe] trend, pointing at Eu having a contribution from progenitors of similar timescales to that of progenitors producing Mg (i.e. SNe II). It has indeed been shown by Travaglio et al. (1999) that SNe II progenitors with masses of 8–10 $M_{\odot}$ best reproduce the r-process enrichment in the Galaxy, and Cescutti et al. (2006) showed that to reproduce the ratio of typical s-process elements, such as [Ba/Fe], at low metallicities, an r-process production of these elements in stars with masses ranging from 8 to 30 $M_{\odot}$ should be assumed. Nonetheless, the origin of r-elements is, as mentioned earlier, still debated (see e.g. Sneden et al. 2000; Thielemann et al. 2011; Côté et al. 2019; Siegel et al. 2019; Kajino et al. 2019).

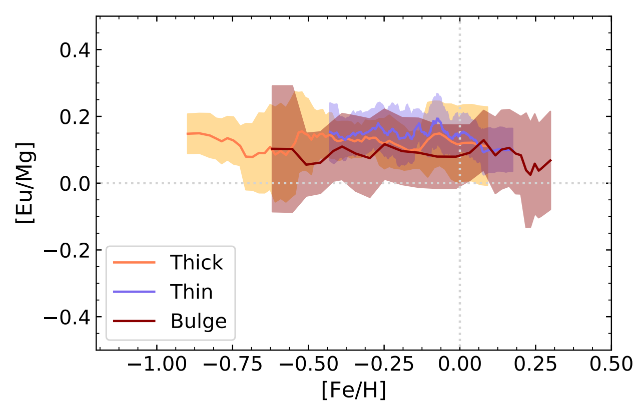

Fig. 8. [Eu/Mg] abundances against [Fe/H] as running mean with a 1σ scatter for the thin disk (blue), thick disk (yellow), and bulge (red).

A way to disentangle the s- and r-process contribution throughout the evolution of the Galaxy is to compare an s-process-dominated element with an r-process-dominated one. We thus compare La, with an s-process contribution of 76%, to

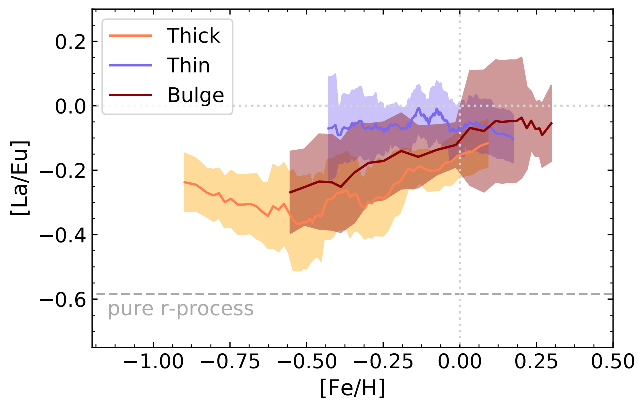

Fig. 9. [La/Eu] abundances against [Fe/H] as running mean with a 1σ scatter for the thin disk (blue), thick disk (yellow), and bulge (red). A pure r-process line is plotted, calculated using the values presented in Bisterzo et al. (2014).

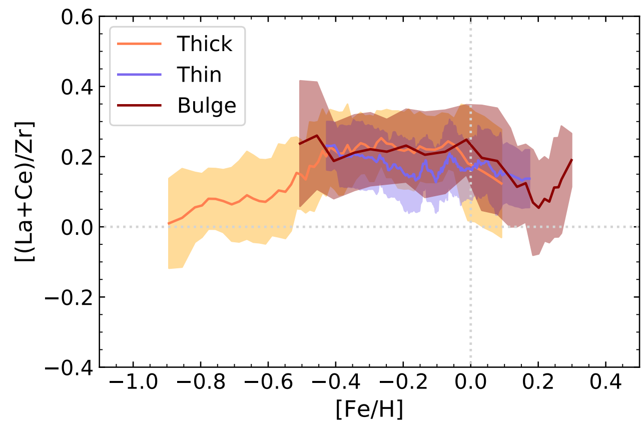

Fig. 10. Abundance ratio of the second-peak s-process elements (La, Ce) and the first-peak s-process element (Zr) against [Fe/H] as running mean with a 1σ scatter for the thin disk (blue), thick disk (yellow), and bulge (red).

that of Eu with an r-process contribution of 94% (Bisterzo et al. 2014), plotted as [La/Eu] in Fig. 9. A pure r-process line is added, using the values from Bisterzo et al. (2014). The value of the pure r-process line is calculated by subtracting the predicted s-process abundance from the solar system total values, that is, by treating the r-process as a residual (Bisterzo et al. 2014).

The trends in Fig. 9 show that the r-process increasingly dominates the production of neutron-capture elements with decreasing metallicity, reaching [La/Eu] = −0.25 for the bulge and [La/Eu] = −0.4 for the thick disk at [Fe/H] ~ −0.5. With regard to the large scatter at supersolar metallicities, we refrain from making any further interpretations of the bulge abundances at these metallicities. At around [Fe/H] ~ −0.6 the [La/Eu] thick disk trend levels off or even increases with lower metallicities. Whether this is significant or not is yet to be understood and observations of more stars in this metallicity range are needed. The generally higher [La/Eu] abundances of the bulge compared with those of the thick disk point at the bulge having either less r-process production (in turn, possibly a different amount of SNe II), or a higher s-process contribution (as seen previously in the [La/Fe]-trend) than that of the thick disk.

5.3. First- and second-peak s-process elements

In Fig. 10, the running mean of the ratio of the second-peak s-process elements (a mean of La and Ce) and the first-peak s-process element Zr are plotted against metallicity. The trend, elaborated on in the last paragraph of this section, can be explained by considering the stellar yields from Karakas & Lugaro (2016), where low-mass AGB stars have a higher relative production of second-peak elements compared to the production of first-peak elements.

The neutrons in the s-process come from two neutron sources: the $^{13}C(\alpha,n)^{16}O$- and the $^{22}Ne(\alpha,n)^{25}Mg$-reactions. The ^{13}C source has a lower neutron density of roughly 10^7 neutrons cm^{-3}, whereas the neutron density for the ^{22}Ne source is around 10^{15} neutrons cm^{-3}. However, due to the longer timescales of the ^{13}C reaction ($\sim10^3$ yr compared to $\sim$10 yr), the time integrated neutron flux for this neutron source is much higher than for the ^{22}Ne source. Due to this, the ^{13}C reaction builds up the heavier s-process elements, such as the second- (and third-)peak elements, whilst the ^{22}Ne reaction is limited to producing the first-peak s-process elements (Karakas & Lattanzio 2014).

Furthermore, Bisterzo et al. (2017) elaborate on the importance of the size of the ^{13}C-pocket in the s-process production. The ^{22}Ne reaction takes place only in initially more massive (AGB) stars of >4 $M_{\odot}$, due to the higher temperatures of these stars (Karakas & Lattanzio 2014). This shrinks the ^{13}C-pocket, resulting in a smaller quantity of s-elements being expected, especially the heavier ones. In short, heavier AGB stars produce relatively fewer second-peak elements compared to low-mass AGB stars, and the latter have a longer time delay.

Another aspect to keep in mind is that at lower metallicities, the ratio of the number of neutrons to the number of available ^{56}Fe-seeds is higher, compared to higher metallicities, which enables the build-up of second-peak elements (Busso et al. 1999).

In Fig. 10 we first see an increasing trend in the thick disk for increasing metallicities, which turns over for solar metallicities and higher. Below solar metallicities (and above [Fe/H] ~ −0.5), all trends show an enrichment of second-peak as compared to first-peak elements. This is therefore explained by the low-mass AGB stars which have not yet enriched the interstellar medium (ISM) at the time of the formation of the older thick disk stars, resulting in relatively low [(La+Ce)/Zr] abundances at early times.

At solar metallicities, the disk populations does not show any clear differences. As for the bulge, it follows the trend of the thick disk more closely than that of the thin disk at subsolar metallicities. At supersolar metallicities, the first-peak elements seem to increase in the bulge, possibly explained by a contribution of metal-rich AGB stars, producing a higher amount of first-peak elements (Karakas & Lugaro 2016).

6. Conclusions

In this work we determined abundances of the neutron-capture elements Zr, La, Ce, and Eu in 45 bulge giants and 291 local disk giants. The determination has been done using high-resolution spectra obtained with FLAMES/UVES (bulge sample) or either FIES or PolarBase (disk sample) and the analysis code SME.

All spectra are evaluated over the wavelength region 5800–6800 Å and the careful, manual definition of the continuum surrounding the spectral lines of interest in the spectra has been crucial in order to get high-precision abundances. Hyperfine splitting (in the cases of La, Eu) has been taken into account, as well as isotopic shifts by manually scaling the log (gf)-values of the identified transitions in the line list (for the isotopes of Zr, Ce, Eu).

The stellar mass and metallicity are factors that contribute to, and affect, the s- and r-process production. Due to this, the enrichment of the ISM and the abundance of neutron-capture elements vary with time in the Galaxy, making them suitable probes for Galactic chemical evolution.

Our [Zr, La, Ce/Fe] bulge trends are in general flatter than those reported by previous studies, many of which are decreasing with higher metallicities. Such decreasing trends would suggest a higher r-process contribution to these elements in the bulge, while our flatter trends that have the same general shapes as our thick disk trends suggest more similar r/s-proportions in the creation of the neutron capture elements in the bulge and disks. The [La/Fe] bulge trend is ~0.1 dex higher compared with the disk, possibly indicating a higher s-process contribution in the bulge, compared with that of the disk.

For [Eu/Fe], we see a decreasing trend with increasing metallicities for both the disk and the bulge, with a plateau at around [Fe/H] ~ -0.4. This is very similar to the typical α-element trend, and plotting [Eu/Mg] confirms this, suggesting that the r-process has a similar production rate as that of Mg (coming from SNe II).

For [La/Eu] we find that towards low metallicities, the abundances lay closer to the pure r-process line (reaching [La/Eu] -0.4 (disk) and -0.25 (bulge) at [Fe/H] ~ -0.5), indicating that the r-process was the dominating neutron-capture process at early times, both in the disk and the bulge. The results also point at either (a) a different amount of massive stars or (b) different contribution of the s-process in the local thick disk and the bulge, where the [La/Eu] abundances seem to be systematically higher in the bulge than in the thick disk. Since we compare abundances determined with the same method, and for stars at the same evolutionary stage, the difference between the disk and the bulge in [La/Fe] could likely be real.

When plotting the ratio of the second- and first-peak s-process elements, [(La+Ce)/Zr], against metallicity we see that the bulge and the thick disk trends follow each other closely. We also show that, according to theoretical predictions by Karakas & Lattanzio (2014), low-mass AGB stars are needed to explain the enhancement of second-peak s-process abundances compared to first-peak s-process abundances.

To conclude, in general, our findings for Zr, Ce and Eu suggest that the bulge experiences a similar chemical evolution to that of the local thick disk, with a similar star formation rate. On the other hand, our La trends for the bulge and the thick disk are offset by about 0.1: systematic effects could not be identified in our homogeneous analysis of the bulge and disk samples and further investigation is still required. Our results for the s-process elements differ substantially from previous studies: here we find flatter trends. More bulge data would be needed to decrease the scatter and put further constraints on bulge abundances. Additionally, it would be useful to adopt the abundances in Galactic Chemical Evolution models to put further constraints on the evolution of the Galaxy and its components.

Acknowledgements. We would like to thank the referee, Mathieu Van der Swaelmen, for very insightful comments and suggestions which helped to improve this paper in many ways. This research has been partly supported by the Lars Hierta Memorial Foundation, and the Royal Physiographic Society in Lund through Stiftelsen Walter Gyllenbergs fond and Märta och Erik Holmbergs donation. H.J. acknowledges support from the Crafoord Foundation, Stiftelsen Olle Engkvist Byggmästare, and Ruth och Nils-Erik Stenbäcks stiftelse. This work has made use of data from the European Space Agency (ESA) mission *Gaia* (`https://www.cosmos.esa.int/gaia`), processed by the *Gaia* Data Processing and Analysis Consortium (DPAC, `https://www.cosmos.esa.int/web/gaia/dpac/consortium`). Funding for the DPAC has been provided by national institutions, in particular the institutions participating in the *Gaia* Multilateral Agreement. This publication made use of the SIMBAD database, operated at CDS, Strasbourg, France; NASA's Astrophysics Data System; and the VALD database, operated at Uppsala University, the Institute of Astronomy RAS in Moscow, and the University of Vienna.

References

Abbott, B. P., Abbott, R., Abbott, T. D., et al. 2017, Phys. Rev. Lett., 119, 161101
Bailer-Jones, C. A. L., Rybizki, J., Fouesneau, M., Mantelet, G., & Andrae, R. 2018, AJ, 156, 58
Ballero, S. K., Matteucci, F., Origlia, L., & Rich, R. M. 2007, A&A, 467, 123
Barbuy, B., Chiappini, C., & Gerhard, O. 2018, ARA&A, 56, 223
Battistini, C., & Bensby, T. 2016, A&A, 586, A49
Bensby, T., Feltzing, S., & Oey, M. S. 2014, A&A, 562, A71
Biemont, E., Grevesse, N., Hannaford, P., & Lowe, R. M. 1981, ApJ, 248, 867
Bisterzo, S., Travaglio, C., Gallino, R., Wiescher, M., & Käppeler, F. 2014, ApJ, 787, 10
Bisterzo, S., Travaglio, C., Wiescher, M., Käppeler, F., & Gallino, R. 2017, ApJ, 835, 97
Brooke, J. S. A., Bernath, P. F., Schmidt, T. W., & Bacskay, G. B. 2013, J. Quant. Spectr. Rad. Transf., 124, 11
Buder, S., Asplund, M., Duong, L., et al. 2018, MNRAS, 478, 4513
Burbidge, E. M., Burbidge, G. R., Fowler, W. A., & Hoyle, F. 1957, Rev. Mod. Phys., 29, 547
Busso, M., Gallino, R., & Wasserburg, G. J. 1999, ARA&A, 37, 239
Cardelli, J. A., Clayton, G. C., & Mathis, J. S. 1989, ApJ, 345, 245
Cescutti, G., François, P., Matteucci, F., Cayrel, R., & Spite, M. 2006, A&A, 448, 557
Chang, T. L., Qian, Q.-Y., Zhao, M.-T., & Wang, J. 1994, Int. J. Mass Spectrom. Ion Process., 139, 95
Chang, T.-L., Qian, Q.-Y., Zhao, M.-T., Wang, J., & Lang, Q.-Y. 1995, Int. J. Mass Spectrom. Ion Process., 142, 125
Côté, B., Eichler, M., Arcones, A., et al. 2019, ApJ, 875, 106
Couch, R. G., Schmiedekamp, A. B., & Arnett, W. D. 1974, ApJ, 190, 95
Cristallo, S., Abia, C., Straniero, O., & Piersanti, L. 2015, ApJ, 801, 53
de Laeter, J. R., & Bukilic, N. 2005, Int. J. Mass Spectrom., 244, 91
Delgado Mena, E., Tsantaki, M., Adibekyan, V. Z., et al. 2017, A&A, 606, A94
Duong, L., Asplund, M., Nataf, D. M., Freeman, K. C., & Ness, M. 2019, MNRAS, 486, 5349
Gaia Collaboration (Prusti, T., et al.) 2016, A&A, 595, A1
Gaia Collaboration (Brown, A. G. A., et al.) 2018, A&A, 616, A1
Gonzalez, O. A., Rejkuba, M., Zoccali, M., et al. 2011, A&A, 530, A54
Gonzalez, O. A., Rejkuba, M., Zoccali, M., et al. 2012, A&A, 543, A13
Gonzalez, O. A., Zoccali, M., Vasquez, S., et al. 2015, A&A, 584, A46
Grevesse, N., Asplund, M., & Sauval, A. J. 2007, Space Sci. Rev., 130, 105
Grevesse, N., Scott, P., Asplund, M., & Sauval, A. J. 2015, A&A, 573, A27
Gruyters, P., Lind, K., Richard, O., et al. 2016, A&A, 589, A61
Guiglion, G., de Laverny, P., Recio-Blanco, A., & Prantzos, N. 2018, A&A, 619, A143
Gustafsson, B., Edvardsson, B., Eriksson, K., et al. 2008, A&A, 486, 951
Hayden, M. R., Bovy, J., Holtzman, J. A., et al. 2015, ApJ, 808, 132
Heiter, U., Lind, K., Asplund, M., et al. 2015, Phys. Scr, 90, 054010
Herwig, F. 2005, ARA&A, 43, 435
Hinkle, K., Wallace, L., Harmer, D., Ayres, T., & Valenti, J. 2000, IAU Joint Discuss., 24, 26
Immeli, A., Samland, M., Gerhard, O., & Westera, P. 2004, A&A, 413, 547
Jofré, P., Heiter, U., Soubiran, C., et al. 2015, A&A, 582, A81
Johnson, C. I., Rich, R. M., Kobayashi, C., & Fulbright, J. P. 2012, ApJ, 749, 175
Jönsson, H., Ryde, N., Nordlander, T., et al. 2017a, A&A, 598, A100
Jönsson, H., Ryde, N., Schultheis, M., & Zoccali, M. 2017b, A&A, 600, C2
Kajino, T., Aoki, W., Balantekin, A. B., et al. 2019, Prog. Part. Nucl. Phys., 107, 109
Karakas, A. I., & Lattanzio, J. C. 2014, PASA, 31, e030

Karakas, A. I., & Lugaro, M. 2016, ApJ, 825, 26
Korn, A. J., Grundahl, F., Richard, O., et al. 2007, ApJ, 671, 402
Kratz, K.-L., Farouqi, K., Pfeiffer, B., et al. 2007, ApJ, 662, 39
Lawler, J. E., Bonvallet, G., & Sneden, C. 2001a, ApJ, 556, 452
Lawler, J. E., Wickliffe, M. E., den Hartog, E. A., & Sneden, C. 2001b, ApJ, 563, 1075
Lawler, J. E., Sneden, C., Cowan, J. J., & Ivans, I. I., & Den Hartog E. A. 2009, ApJS, 182, 51
Lecureur, A., Hill, V., Zoccali, M., et al. 2007, A&A, 465, 799
Lind, K., Korn, A. J., Barklem, P. S., & Grundahl, F. 2008, A&A, 490, 777
Lind, K., Bergemann, M., & Asplund, M. 2012, MNRAS, 427, 50
Liu, F., Asplund, M., Yong, D., et al. 2019, A&A, 627, A117
Lomaeva, M., Jönsson, H., Ryde, N., Schultheis, M., & Thorsbro, B. 2019, A&A, 625, A141
Marquardt, D. W. 1963, J. Soc. Ind. Appl. Math., 11, 431
Mashonkina, L., & Gehren, T. 2000, A&A, 364, 249
Matteucci, F., & Brocato, E. 1990, ApJ, 365, 539
Matteucci, F., Grisoni, V., Spitoni, E., et al. 2019, MNRAS, 487, 5363
McMillan, P. J. 2018, Res. Notes AAS, 2, 51
McWilliam, A. 2016, PASA, 33, e040
Meléndez, J., Asplund, M., Alves-Brito, A., et al. 2008, A&A, 484, L21
Mishenina, T. V., Pignatari, M., Korotin, S. A., et al. 2013, A&A, 552, A128
Nomura, M., Kogure, K., & Okamoto, M. 1983, Int. J. Mass Spectrom. Ion Process., 50, 219
Nordlander, T., Korn, A. J., Richard, O., & Lind, K. 2012, ApJ, 753, 48
Pedregosa, F., Varoquaux, G., Gramfort, A., et al. 2011, J. Mach. Learn. Res., 12, 2825
Petit, P., Louge, T., Théado, S., et al. 2014, PASP, 126, 469
Piskunov, N., & Valenti, J. A. 2017, A&A, 597, A16
Portail, M., Gerhard, O., Wegg, C., & Ness, M. 2017, MNRAS, 465, 1621
Prochaska, J. X., & McWilliam, A. 2000, ApJ, 537, L57
Shen, J., & Li, Z.-Y. 2016, in Galactic Bulges, eds. E. Laurikainen, R. Peletier, & D. Gadotti (Berlin: Springer), 418, 233
Siegel, D. M., Barnes, J., & Metzger, B. D. 2019, Nature, 569, 241
Sneden, C., Cowan, J. J., Ivans, I. I., et al. 2000, ApJ, 533, L139
Sneden, C., Lucatello, S., Ram, R. S., Brooke, J. S. A., & Bernath, P. 2014, ApJS, 214, 26
Souto, D., Allende Prieto, C., Cunha, K., et al. 2019, ApJ, 874, 97
Telting, J. H., Avila, G., Buchhave, L., et al. 2014, Astron. Nachr., 335, 41
Thielemann, F.-K., Arcones, A., Käppeli, R., et al. 2011, Prog. Part. Nucl. Phys., 66, 346
Thielemann, F. K., Eichler, M., Panov, I. V., & Wehmeyer, B. 2017, Ann. Rev. Nucl. Part. Sci., 67, 253
Thielemann, F.-K., Isern, J., Perego, A., & von Ballmoos, P. 2018, Space Sci. Rev., 214, 62
Thorsbro, B., Ryde, N., Schultheis, M., et al. 2018, ApJ, 866, 52
Thygesen, A. O., Frandsen, S., Bruntt, H., et al. 2012, A&A, 543, A160
Travaglio, C., Galli, D., Gallino, R., et al. 1999, ApJ, 521, 691
Travaglio, C., Gallino, R., Arnone, E., et al. 2004, ApJ, 601, 864
Valenti, J. A., & Piskunov, N. 1996, A&AS, 118, 595
Van der Swaelmen, M., Barbuy, B., Hill, V., et al. 2016, A&A, 586, A1
Velichko, A. B., Mashonkina, L. I., & Nilsson, H. 2010, Astron. Lett., 36, 664
Wegg, C., Gerhard, O., & Portail, M. 2015, MNRAS, 450, 4050
Weiland, J. L., Arendt, R. G., Berriman, G. B., et al. 1994, ApJ, 425, L81
Zasowski, G., Schultheis, M., Hasselquist, S., et al. 2019, ApJ, 870, 138

Appendix A: Additional tables

Table A.1. Basic data for the observed bulge giants.

Star [(a)]	RA (J2000) (h:m:s)	Dec (J2000) (d:am:as)	V	S/N
SW-09	17:59:04.533	−29:10:36.53	16.153	16
SW-15	17:59:04.753	−29:12:14.77	16.326	15
SW-17	17:59:08.138	−29:11:20.10	16.388	11
SW-18	17:59:06.455	−29:10:30.53	16.410	14
SW-27	17:59:04.457	−29:10:20.67	16.484	13
SW-28	17:59:07.005	−29:13:11.35	16.485	16
SW-33	17:59:03.331	−29:10:25.60	16.549	14
SW-34	17:58:54.418	−29:11:19.82	16.559	12
SW-43	17:59:04.059	−29:13:30.26	16.606	16
SW-71	17:58:58.257	−29:12:56.97	16.892	14

Notes. The S/N per data point is measured by the IDL-routine `der_snr.pro`, see `http://www.stecf.org/software/ASTROsoft/DER_SNR`. [(a)]Using the same naming convention as Lecureur et al. (2007) for the B3-BW-B6-BL-stars. This is only an excerpt of the table to show its form and content. The complete table is available in electronic form at the CDS.

Table A.2. Basic data for the observed solar neighbourhood giants.

HIP/KIC/TYC	Alternative name	RA (J2000) (h:m:s)	Dec (J2000) (d:am:as)	V	v_{rad} km s^{-1}	S/N	Source
HIP1692	HD1690	00:21:13.32713	−08:16:52.1625	9.18	18.37	114	FIES-archive
HIP9884	alfAri	02:07:10.40570	+23:27:44.7032	2.01	−14.29	90	PolarBase
HIP10085	HD13189	02:09:40.17260	+32:18:59.1649	7.56	26.21	156	FIES-archive
HIP12247	81Cet	02:37:41.80105	−03:23:46.2201	5.66	9.34	176	FIES-archive
HIP28417	HD40460	06:00:06.03883	+27:16:19.8614	6.62	100.64	121	PolarBase
HIP33827	HR2581	07:01:21.41827	+70:48:29.8674	5.69	−17.99	79	PolarBase
HIP35759	HD57470	07:22:33.85798	+29:49:27.6626	7.67	−30.19	85	PolarBase
HIP37447	alfMon	07:41:14.83257	−09:33:04.0711	3.93	11.83	71	Thygesen et al. (2012)
HIP37826	betGem	07:45:18.94987	+28:01:34.3160	1.14	3.83	90	PolarBase
HIP43813	zetHya	08:55:23.62614	+05:56:44.0354	3.10	23.37	147	PolarBase

Notes. Coordinates and magnitudes are taken from the SIMBAD database, while the radial velocities are measured from the spectra. The S/N per data point is measured by the IDL-routine `der_snr.pro`, see `http://www.stecf.org/software/ASTROsoft/DER_SNR`. This is only an excerpt of the table to show its form and content. The complete table is available in electronic form at the CDS.

Table A.3. Stellar parameters and determined abundances for observed bulge giants.

Star	T_{eff}	$\log g$	[Fe/H]	v_{micro}	A(Zr)	A(La)	A(Ce)	A(Eu)
SW-09	4095	1.79	−0.15	1.32	2.79	1.09	1.72	0.75
SW-15	4741	1.96	−0.98	1.62	...	...	1.51	...
SW-17	4245	2.09	0.24	1.44	2.95	1.26	...	0.97
SW-18	4212	1.67	−0.13	1.49	2.30	0.84	1.86	0.86
SW-27	4423	2.34	0.11	1.60	2.73	1.22	2.09	1.05
SW-28	4254	2.36	−0.14	1.44	2.26	1.42	2.45	0.91
SW-33	4580	2.72	0.16	1.39	2.55	1.60	2.29	1.05
SW-34	4468	1.75	−0.45	1.63	2.34	1.04	...	...
SW-43	4892	2.34	−0.77	1.84	...	0.75	...	0.28
SW-71	4344	2.66	0.39	1.31	3.10	1.77	...	...

Notes. [Fe/H] is listed in the scale of Grevesse et al. (2015). This is only an excerpt of the table to show its form and content. The complete table is available in electronic form at the CDS.

Table A.4. Stellar parameters and determined abundances for observed solar neighbourhood giants.

HIP/KIC/TYC	T_{eff}	$\log g$	[Fe/H]	v_{micro}	A(Zr)	A(La)	A(Ce)	A(Eu)
HIP1692	4216	1.79	−0.26	1.55	2.20	0.97	1.41	0.51
HIP9884	4464	2.27	−0.21	1.34	2.34	1.08	1.55	0.53
HIP10085	4062	1.44	−0.32	1.63	2.32	1.03	1.48	0.51
HIP12247	4790	2.71	−0.04	1.40	2.57	1.28	1.74	0.63
HIP28417	4746	2.56	−0.25	1.40	2.24	1.02	1.39	0.52
HIP33827	4235	1.99	0.01	1.50	2.61	1.23	1.68	0.72
HIP35759	4606	2.47	−0.15	1.42	2.23	1.06	1.54	0.74
HIP37447	4758	2.73	−0.04	1.35	2.49	1.26	1.75	0.71
HIP37826	4835	2.93	0.07	1.24	2.68	1.33	1.79	0.73
HIP43813	4873	2.62	−0.07	1.51	2.61	1.35	1.83	0.63

Notes. [Fe/H] is listed in the scale of Grevesse et al. (2015). This is only an excerpt of the table to show its form and content. The complete table is available in electronic form at the CDS.